universität wien

DISSERTATION / DOCTORAL THESIS

Titel der Dissertation / Title of the Doctoral Thesis

Atomic scale dynamics and modifications of stacked heteronanostructures under extreme conditions

verfasst von / submitted by

Heena Inani

angestrebter akademischer Grad / in partial fulfilment of the requirements for the degree of

Doktorin der Naturwissenschaften (Dr. rer. nat.)

Wien, 2021 / Vienna, 2021

Studienkennzahl lt. Studienblatt / degree programme code as it appears on the student record sheet:	UA 796 605 411
Dissertationsgebiet lt. Studienblatt / degree programme as it appears on the student record sheet:	Physik
Betreut von / Supervisor:	Assoc. Prof. Dr. Jani Kotakoski

Abstract

Since the discovery of atomically thin graphene, low-dimensional materials are making rapid progress for their use in future technology due to their exceptional intrinsic properties. Atomically thin nature of materials allows us to extrinsically introduce atomic scale modifications, hence manipulate the properties for particular application. The external manipulation processes are also important for optimizing the materials sustainability in device operations. There is a broad range of methods to externally modify materials, for example, the application of electric field, high temperatures, gaseous and liquid environment, electron and particle irradiation etc. The high-end electron microscopes with $\mathring{A}$-level resolution and customized with tools made it possible to study the atomic structure of materials and test them under various environments which provide insights into structural dynamics and transformation of materials.

This thesis presents the structural modifications in 1D (carbon nanotubes), 2D (graphene, MoS_2) and their stacked systems under external stimuli such as electric biasing, plasma and highly charged ion irradiation by employing scanning transmission electron microscopy (STEM). In this thesis, I modified the target materials using various methods and performed *in situ* and *ex situ* experiments for observing the structural dynamics and evolution. Firstly, we used Ar plasma irradiation method to substitute heteroatoms (Si) in both graphene and SWCNTs lattices. The results reveal that the Si atoms are found in 3-fold and 4-fold configurations in SWCNTs. Secondly, we studied the effect of highly charged ions on graphene-MoS_2 heterostructrues. The results show that irradiation leads to the creation of nanosize pores in MoS_2, while graphene lattice remains intact. In an experiment, when sample is irradiated on graphene side, both lattices remain unaffected. Finally, we performed *in situ* Joule-heating experiments on graphene and graphene-MoS_2 heterostructrues. The results exhibits dynamics, transformation and evaporation of contaminants on graphene lattice while the temperature reaches up to 2000 K and beyond depending on device geometry. In the case of a heterostructure, at a bias of 3 V over the suspended sample, we observed the gradual transformation of 2D MoS_2 into 3D nanocrystals followed by processes such as vacancy formation, void expansion and edge evaporation.

In summary, this work explored the different methods to structurally modify the multidimensional heterostructures (1D/2D and 2D/2D) and could be extended to entire range of low-dimensional materials and their stack combinations to get insights into growth, dynamics and evolution of materials and establish new nanofabrication technique.

Zusammenfassung

Seit der Entdeckung von Graphen haben niedrigdimensionale Materialien große Fortschritte in Richtung Verwendung in zukünftigen Technologien aufgrund ihrer einzigartigen Eigenschaften gemacht. Durch ihre Zweidimensionalität ist es möglich Veränderungen auf atomarer Ebene durchzuführen und damit Eigenschaften für bestimmte Einsatzzwecke maßzuschneidern. Die verwendete Methode ist auch entscheidend für die Zuverlässigkeit der Materialien bei ihrer Anwendung. Es existieren verschiedenste Möglichkeiten, um Materialien zu verändern, z.B. elektrische Felder, Gase und Flüssigkeiten, sowie diverse Teilchen wie Elektronen etc. Elektronenmikroskope mit Auflösung im Angstrom-Bereich erlauben es atomare Strukturen zu untersuchen und unter verschiedensten Bedingungen zu testen. Dies dient zur Gewinnung von Erkenntnissen über Dynamiken und Transformationen in Materialien. Diese Dissertation zeigt Strukturänderungen in 1D (Kohlenstoffnanoröhrchen), 2D (Graphen, MoS_2) und deren gestapelten Systemen mittels Rastertransmissionselektronenmikroskopie. Diese Veränderungen wurden durch externe Einflüsse wie elektrischer Spannung, Plasma- und Ionenbestrahlung erzeugt. Die verwendeten Materialien wurden mit verschiedensten Methoden verändert. Es wurden *in situ* sowie *ex situ* Experimente durchgeführt, um Strukturdynamiken zu beobachten. Zuerst wurde Argonplasma verwendet, um Siliziumheteroatome in Graphen und SWCNTs zu substituieren. Die Ergebnisse zeigen, dass Siliziumatome sowohl in 3- als auch 4-koordinierter Bindung vorliegen können. Außerdem wurden die Auswirkungen von Ionenbestrahlung auf Graphen-MoS_2 Heterostrukturen untersucht. Die Ergebnisse zeigen, dass die Bestrahlung zur Erzeugung von Nanoporen in MoS_2 führen. Im Gegensatz dazu bleibt Graphen intakt. Wenn die Heterostruktur auf der Graphenseite bestrahlt wird, entstehen indes keine Poren. Abschließend wurden Heizexperimente mit Graphen und Graphen-MoS_2 Heterostrukturen durchgeführt. Die Ergebnisse zeigen die Dynamiken und Verdampfung von Verunreinigungen auf Graphen bei Temperaturen von über 2000 K in Abhängigkeit der Probengeometrie. Im Fall der Heterostruktur wurde bei einer Vorspannung von 3 V die Transformation von 2D MoS_2 in einen 3D Nanokristall beobachtet. Zusammenfassend, diese Arbeit untersucht verschiedene Methoden, um Strukturänderungen in mehrfachdimensionalen (1D/2D und 2D/2D) Heterostrukturen zu induzieren. Diese können für eine breite Palette (gestapelter) niedrigdimensionaler Materialien verwendet werden, um Einsicht in Wachstum und Dynamiken dieser zu bekommen. Außerdem dienen die gewonnenen Erkenntnisse zur Entwicklung neuer Methoden für die Nanofabrikation.

Acknowledgements

Throughout this journey of my PhD I have received a great deal of support from many people, without whom I would not have been able to come this far and write this thesis. First and foremost, I would like to express my sincere gratitude to my PhD supervisor, Prof. Jani Kotakoski for his constant support, guidance and encouragement, and also for generously giving me opportunities to attend international conferences and to collaborate with diverse research groups. His attentive supervision, expertise in the field of electron microscopy, suggestions and ideas were invaluable in formulating my research. I am extremely grateful to him for being kind, always be there to listen my work-related concerns and provide solutions throughout the course of my PhD.

I would like to extend my similar sincere gratitude to Dr. Kimmo Mustonen for his support and assistance during each research project. His positive attitude and encouraging words helped me a lot to believe in myself and to be motivated during my PhD. I feel blessed to get opportunity to learn from Prof. Jani Kotakoski and Dr. Kimmo Mustonen. Thanks to their collective support and guidance I did not only broaden my scientific knowledge but I was also encouraged to learn and improve other skills including academic writing and computer programming. Furthermore, I am extremely thankful to Dr. Clemens Mangler for his unmatchable dedication to ensure the great performance of STEM machine and always be there to help me out with any problem during experiments.

I would like to thank my former and current colleagues Dr. Viera Skakalova, Dr. Alexander Markevich, Prof. Toma Susi, Dr. Jacob Madsen, Dr. Mohammad Monazam, Dr. Ursula Ludacka, Alex Chirita, Rajendra Singh, Alberto Trentino, Thuy An Bui, Manuel Längle and Dr. Harriet Åhlgren, for their support. A special mention and thanks goes to Dr. Mukesh Tripathi and Georg Zagler for helping me out with administrative stuff at the beginning of my PhD, and Gregor Leuthner for translation of the abstract of this thesis into German. I would like to thank Ms. Regina Pinter and Ms. Kathrin Linke for all administrative support. I would also like to thank Vienna Doctoral School in Physics (VDSP) for providing a great platform and support for both personal and professional development. Last but not least, I am extremely grateful to god, my family and friends for their unconditional love and support. Special thanks and mention to my parents, who gave me freedom to follow my dreams, never questioned my life choices and supported me at every stage.

Contents

List of acronyms

0D zero-dimensional

1D one-dimensional

2D two-dimensional

3D three-dimensional

TMDs transition metal dichalcogenides

vdWHs van der Waals heterostructures

MoS_2 molybdenum disulfide

WS_2 tungsten diulfide

SWCNT single walled carbon nanotube

MWCNT multi walled carbon nanotube

INT inorganic nanotube

HCI highly charged ions

CFEG cold field emission gun

TEM transmission electron microscopy

STEM scanning transmission electron microscopy

UHV ultra high vacuum

BF bright field

CCD charged-coupled device

ADF annular dark field

MAADF medium angle annular dark field

HAADF high angle annular dark field

EELS electron energy loss spectroscopy

ZLP zero loss peak

FFT fast fourier transform

IPA isopropyl alcohol

PMMA Poly (methyl 2-methylpropenoate)

C$_c$ chromatic aberration

C$_s$ spherical aberration

DFT density functional theory

CVD chemical vapor deposition

EBIT electron beam ion traps

ECRI electron cyclotron resonance ion source

RF radio frequency

EMCCD electron multiplying charge-coupled device

SiN silicon nitride

TP thermophoretic precipitator

GB grain boundary

Chapter 1

Introduction

In low-dimensional materials at least one spatial dimension is small enough so that their properties differ from their bulk counterparts due to quantum confinement. One-dimensional (1D) materials are such as nanotubes, nanowires and nanorods, in which the electronic wave function is confined only in one dimension. Two-dimensional (2D) materials are in form of in-plane bonded atoms. Graphene, for example, is a sheet of carbon atoms in which they form bonds only in two dimensions and particles like electrons can move only in lateral direction i.e. side-to-side, back-to-front or diagonally but not up-down. Over 70 years ago, Peierls [1] and Landau [2] speculated the thermodynamic instability of strict two-dimensional crystals at finite temperatures, thus the existence of suspended 2D materials was not anticipated. In a theoretical study they described that the thermal fluctuations lead to displacement which are of the same magnitude as the interatomic distances and could destroy long-range order [3], making the crystal unstable at finite temperatures. Later, numerous experimental studies showed that thin films below a certain thicknesses become unstable and form islands or even decompose [4, 5]. However, the existence of atomically thin crystals was first demonstrated in 2004 when two scientists from University of Manchester, Andre Geim and Konstantin Novoselov, were exploring the use of graphite (a layered structure consisting of carbon) in transistors. After a series of trial and error, they succeeded in thinning graphite to one layer thereby creating a new material, an atomically thin layer of carbon called graphene [6]. This experiment turned out to be a breakthrough and resulted in them winning the Noble prize in Physics in 2010. The event sparked a quest for establishing the structure and properties of further 2D structures that have since identified in great numbers. Today, many families of 2D materials are known, such as transition metal dichalcogenides (TMDs) and MXenes which are both three atoms thick in contrast to one-atom-thick graphene.

Each individual material has its own unique properties. Additionally, the combination of materials allows us to exploit the properties of two or more materials simultaneously. Because this true low-dimensional materials have no open bonds, they bind only via the weak van der Waals interaction but their electron orbitals are still sufficiently close that, for instance, interlayer excitons may emerge. These combined materials are called van der Waals heterostructures (van der Waals heterostructures (vdWHs)). Despite the weakness of the interactions, they can affect the carrier concentrations and the structure of each of the constituent materials [7, 8]. These stacked systems have become invaluable in fundamental physics research [9, 10, 11]. However, to realize their potential and for applications, it is also important to explore the effects of external stimuli such as elevated temperatures, particle irradiation, electric biasing on them.

Although graphene and single-walled carbon nanotubes posses exceptional properties, their modification has been of great interest for tailoring them to specific applications. Apart from graphene, other 2D materials such as TMDs exhibit fantastic electronic and optical properties of their own. Similar to graphene, atomically thin nature of these materials make them sensitive to atomic scale modifications which could lead to different behavior of them in external stimuli. Such as gaseous environment, high temperatures and electric fields, or transformation into something new. Post-growth modification is a way to efficiently manipulate materials in a controllable manner for desired applications. This can be done for example using particle irradiation or heat treatment, as will be shown in this thesis.

Most viable and environmentally stable method is to covalently incorporate foreign atoms into the lattice. So far, atomic scale observations have demonstrated the incorporation of boron (B), nitrogen (N) and phosphorus (P) in both graphene and single-walled carbon nanotubes (SWCNT) [12, 13, 14, 15]. Substitution of heavy atoms e.g. silicon (Si) [16] and germanium (Ge) [17] has also been reported into graphene lattice. In contrast, there have not been many studies on substitution of heavier atoms into SWCNT lattice, and atomic scale verification via direct imaging is often lacking. A further method is to expose the materials to highly charged ions (HCI). Slow highly charged ions carry large amounts of potential energy, which is released on the surface of a material during the de-excitation of ions. This leads to electronic excitation and ionization on the surface and can lead to the creation of nanostructures. For example, HCI irradiation of TMDs tend to create nanosize pores within layers [18] while graphene due to its high conductivity reportedly remains unaffected [19]. Clearly, different materials are subject to different dynamical processes under HCI irradiation. Several studies also have shown the defect production, phase transformation and edge engineering in materials (black phosphorus and TMDs

etc.) under electron irradiation and at high temperatures [20, 21, 22, 23, 24, 25]. Until now the most of studies have been on an individual material which demands the exploration for two or more materials system. Recently, Tai et al. have shown high temperature and electron irradiation effects on bilayer TMDs systems [26]. However, hetero-stacked systems haven't been explored yet.

The aim of this thesis is to study the influence of extreme conditions such as joule heating, plasma and highly charged ion irradiation on the atomic structure of hetero-stacked system of materials. The main research tool employed in this work is *in situ* scanning transmission electron microscopy.

1.1 Materials

1.1.1 2D materials

Graphene

In 1947, P. Wallace described the band theory of graphene by tight binding model that allows electron hopping only with nearest neighbors [27]. Graphene is an atomically thin sheet of carbon atoms, arranged in a honeycomb lattice shown in Fig. 1.1. It is well known for its exceptional electric, thermal and mechanical properties that emerge on one hand from the strong σ-electron bonds, and on the other hand, from the delocalized π-electrons forming a 2D electron gas [6, 28, 29]. This thin sheet of carbon atoms can be isolated from graphite by overcoming the weak van der Waals interaction between the atomic layers [30].

To explain van der Waals (or π-electron) interaction, one needs to understand the structure of the material. Graphene lattice consists of two interpenetrating triangular lattices (sublattices) shown with two different colours in Fig. 1.1. The primitive lattice vectors are

$$\vec{a_1} = a/2(3,\ \sqrt{3}) \text{ and } \vec{a_2} = a/2(3,\ -\sqrt{3}),$$

where a $= 0.142$ nm, carbon-carbon distance and lattice vectors in reciprocal space are

$$\vec{b_1} = 2\pi/3a(1,\ \sqrt{3}) \text{ and } \vec{b_2} = 2\pi/3a(1,\ -\sqrt{3}).$$

Each carbon atom has four valence electrons. In graphene, three of them form strong in-plane covalent bonds (σ bonds) with the nearest carbon atoms. They are aligned at 120° with each

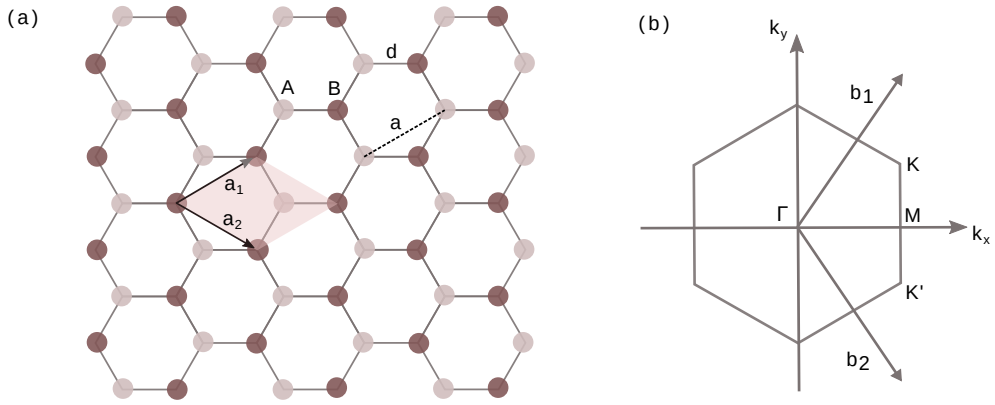

Figure 1.1: (a) The atomic structure of graphene: composed of two unquivalent lattice positions marked with A and B. The unit cell is represented by two primitive lattice vectors $\vec{a_1}$ and $\vec{a_2}$. The lattice constant a is 0.246 nm and the interatomic distance d is 0.142 nm. (b) First Brillouin zone of the graphene lattice with the basis vectors $\vec{b_1}$ and $\vec{b_2}$ of reciprocal space where K and K' are known as Dirac points.

other and hence form a hexagonal structure. The rigidity of these bonds is responsible for the exceptional mechanical properties of graphene. The remaining out-of-plane p_z orbitals of the neighbouring atoms each containing one electron combines to form delocalized π bands [31]. The π orbitals form the valence band and conduction band that meet at the Dirac point exactly where the Fermi energy of graphene lies. This unusual energy dispersion relation makes graphene a zero band gap semiconductor with exactly zero available states in the ground state. The energy spectrum in graphene [32] shows a conical shape close to Fermi energy (Fig. 1.2) which can be represented by the following relation $E = \pm v_f p$ where v_f is Fermi velocity, p is momentum and E is energy. The value of v_f is 10^6 ms^{-1} for graphene.

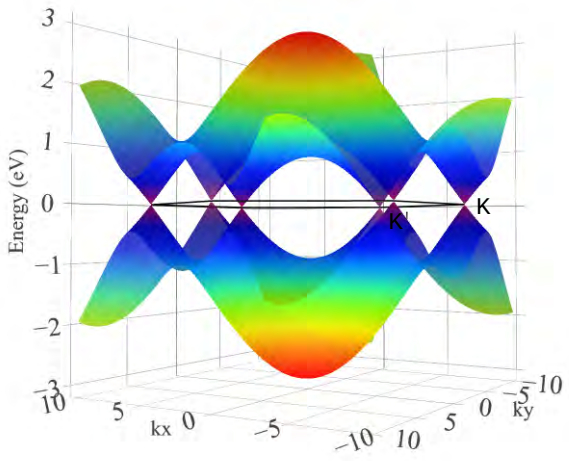

Figure 1.2: Electronic band structure of graphene.

Additionally, suspended graphene has high thermal conductivity of up to 4000 W.m^{-1}.K^{-1} at room temperatures [33, 34], which makes it a really good thermal conductor and it can sustain high temperatures [35].

Molybdenum disulfide (MoS_2)

Transition metal dichalcogenides (TMDs) are of type MX_2 where M is metal (Mo, W, Nb etc.) and X is chalcogen (S, Se, Te) shown in Fig. 1.3, where a metallic plane (molybdenum) is sandwiched between two chalcogen (sulfur) atomic planes. Depending on the stacking of metal and chalcogen planes, TMDs exhibit different structural phases.

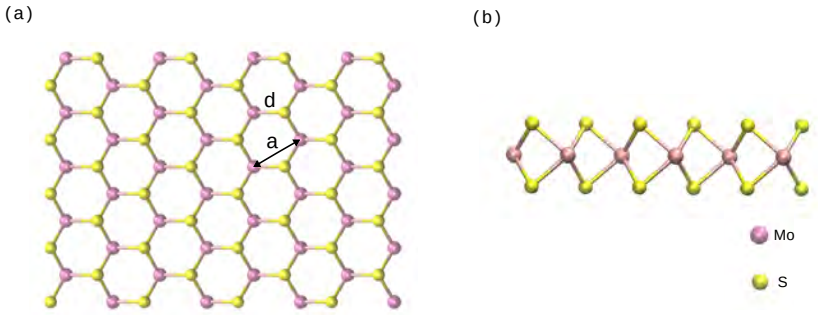

Figure 1.3: The atomic structure of MoS_2 (a) Top view. The lattice constant a is 0.316 nm. The Mo-S distance d is 0.241 nm. (b) Side view in which Mo atomic plane is sandwiched between S atomic planes.

TMDs have properties that are quite different from graphene. These three atom thick materials exhibit, for instance, a direct (intermediate) band gap, strong spin-orbital coupling and optical and mechanical properties suitable for a host of applications [36]. The finite band gap that coinciding with the radiant spectrum of the sun, $h\nu = 1.5$-2.5 eV, renders them useful for energy harvesting applications [37], but also for optoelectronics [38] and for consumer electronics [39], and catalysis [40] etc. The properties of TMDs can depend on the number of layers. For example, some transform from indirect band gap to direct band gap semiconductors upon transition of bulk to monolayer [41]. In this family, MoS_2 is the most studied material due to its robustness, electrical, optical and mechanical properties [42]. Fig. 1.4(a-c) shows the most common phases of monolayer MoS_2: semiconducting 1H, metallic 1T and semi-metallic 1T'. In 1H and 1T, X-M-X configuration is in ABA and ABA' stacking, respectively. Whereas, 1T' is a distorted form of the 1T phase. Bilayer MoS_2 exhibits different phases depending on intralayer stacking (Fig. 1.4(d-e)). For example, 2H and 3R phases are formed by stacking two 1H layers. Transitional zone (TZ) can be formed through sliding of layers.

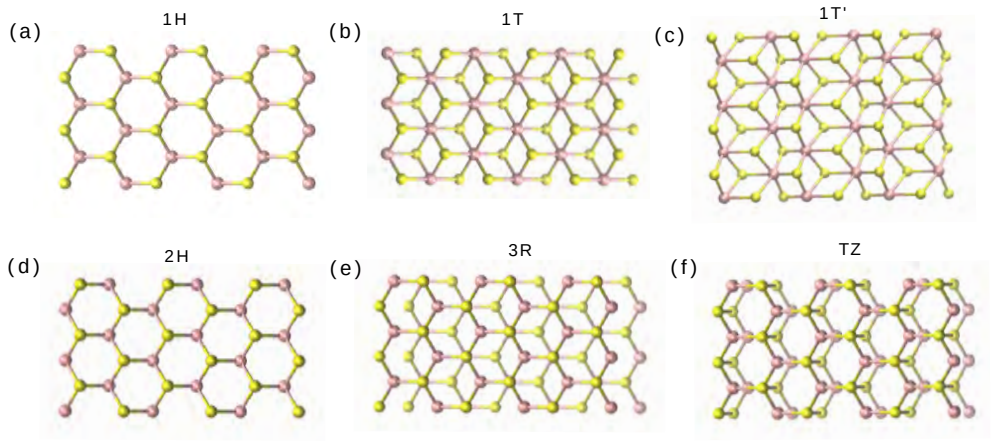

Figure 1.4: **Atomic model of monolayer and bilayer MoS_2 structural phases and polymorphs.** (a) 1H (b) 1T (c) 1T' (d) 2H (e) 3R and (f) transitional zone (TZ) stacking.

1.1.2 1D materials

Carbon nanotubes

A rolled up sheet of graphene can form a hollow cylinder with a diameter in the range of nanometers, known as carbon nanotubes (CNTs). Although accidental observations were made by several researchers earlier, in 1991 Sumio Iijima became the first to describe the atomic structure [43]. CNTs can consist either of a single sheet of graphene and hence dubbed as single-walled carbon nanotubes (SWCNT), or of multiple concentric shells that are called multi walled carbon nanotubes (MWCNT). Despite being made of graphene which is a zero band gap semiconductor, nanotubes exhibit either metallic or semiconducting behavior, depending on the direction a sheet is rolled to form the tubule [44]. The atomic structure and configuration of nanotubes can be described by two integers (n,m). Fig. 1.5 shows the graphene lattice with two basis vectors $\vec{a_1}$ and $\vec{a_2}$ and the chiral vector $\vec{c_h}$

$$\vec{c_h} = n\vec{a_1} + m\vec{a_2}.$$

Nanotubes can be classified into three categories based on (n,m):

1. Zigzag SWCNTs (if $n = 0$ or $m = 0$)
2. Armchair SWCNTs (if $n{=}m$)
3. Chiral SWCNTs (all other n,m)

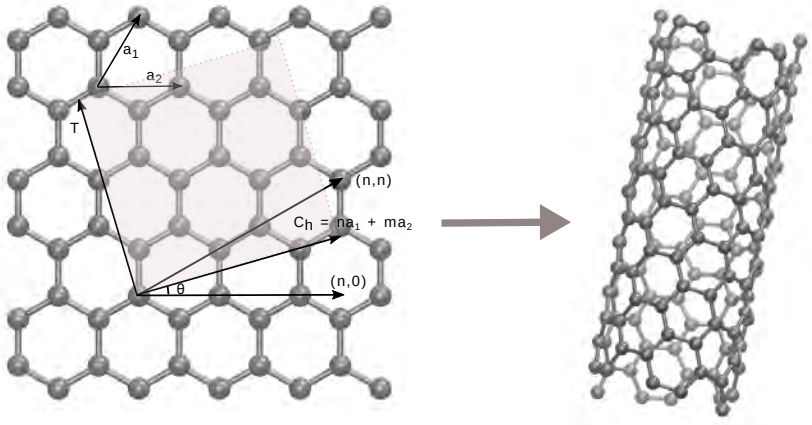

Figure 1.5: A schematic of a 2D graphene sheet showing lattice vectors $\vec{a_1}$ and $\vec{a_2}$, and the roll-up chiral vector $\vec{c_h}$. The lines indicating integers $(n,0)$ and (n,n) form zig-zag and armchair nanotubes, respectively. The shaded box shows the unit cell formed by transnational vector $\vec{T}$ and $\vec{c_h}$. The transnational vector $\vec{T}$ is along the nanotube axis. The molecular model on the right represents the structure of a (6,4) SWCNT.

Armchair SWCNTs exhibit metallic behavior, those with $n-m = 3k$, where k is a non-zero integer are semiconducting with a very small band gap and all others are semiconducting with a band gap that roughly follows $E_{gap} \propto 1/\mathrm{d}_{tube}$, d is the diameter of nanotube. To understand the electronic behavior of nanotubes, we consider the 2D energy dispersion of graphene in which valence and conduction bands touch at six K points defined as the corners of first Brillouin zone (Fig. 1.2). When a finite 2D sheet is rolled up to form a 1D tube, the periodic conditions for allowed 1D subbands are given by: $c_h.\mathrm{k} = 2\pi q$, where q is an integer and c_h is a chiral vector. If the allowed subbands meet with one of the K points then the tube is metallic otherwise semiconducting [44]. Different structures of SWCNTs are shown in Fig. 1.6.

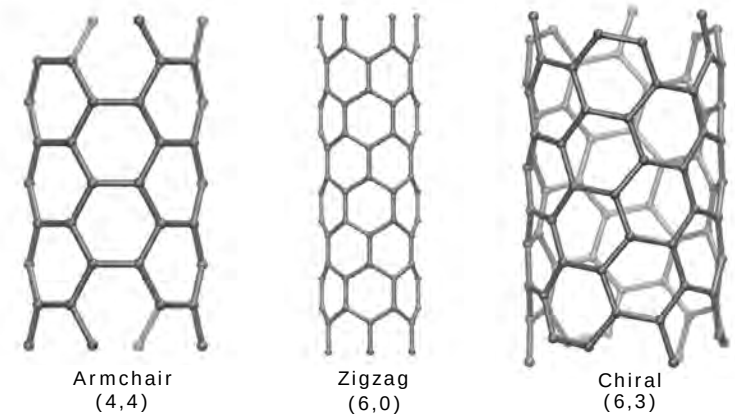

Figure 1.6: Atomic models of (a) an armchair nanotube (b) a zig-zag nanotube and (c) a chiral nanotube.

Inorganic (WS_2) nanotubes

Analogous to graphene, also inorganic 2D materials such as boron nitride (BN) and TMDs (MoS_2, WS_2) can form tubular structures called inorganic nanotubes (INTs). Like CNTs, such tubes also show different structural configurations based on the rolling-up direction. However, INTs do not have a metallic phase but are all semiconducting with a finite band gap regardless of their chirality. INTs can be used in optoelectronics [45, 46] and electronic devices [47, 48]. Fig. 1.7 shows an atomically resolved image of multiwalled WS_2 nanotube. This image was acquired by scanning transmission electron microscope (STEM) and represents an annular dark field (ADF) image taken with high-angle ADF (HAADF) detector, technique and imaging method is described later in section 2.1.1. Although WS_2 NT-graphene heterostructures were studied during the research project that resulted in this thesis, these studies did not lead to significant new knowledge and are therefore not discussed further.

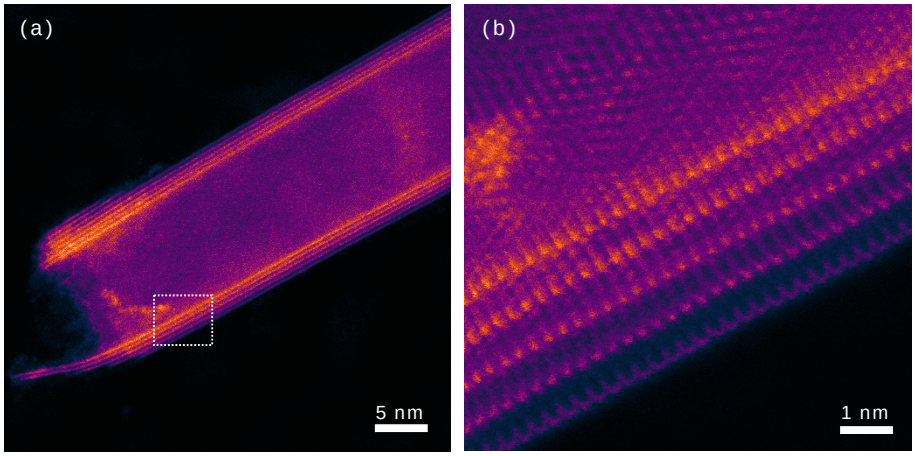

Figure 1.7: A STEM-HAADF image of (a) WS_2 multiwalled nanotube and the (b) atomic structure of nanotube walls from the area selected with white box in panel (a).

1.1.3 Van der Waals heterostructures

Vertical stacking of low-dimensional molecules in which the electron wavefunctions are confined in some (but differing) spatial dimensions, lead into the formation of multidimensional van der Waals heterostructures [49, 50, 11]. Liu et al., for instance, have illustrated the assembly of multidimensional materials and artificial building blocks [50]. Fig. 1.8 shows the atomic scale images of stacked systems of graphene-MoS_2 and graphene-SWCNTs, which are taken with medium angle ADF detector in STEM (described in section 2.1.1). The proximity of the electron orbitals and difference in Fermi level lead to charge transfer, structural reconstruction and proximity ef-

fects [8], leading thereby to a system with new properties. For example, carbon nanotubes arrange themselves in a particular direction on graphene due to the π-π stacking force [51], whereas in graphene-MoS_2 stacks the difference in Fermi level lead into electron transfer between the two molecules [52] etc. Heterostacked systems are promising candidates for energy storage [53], photodetectors [54] and solar cells [55, 56].

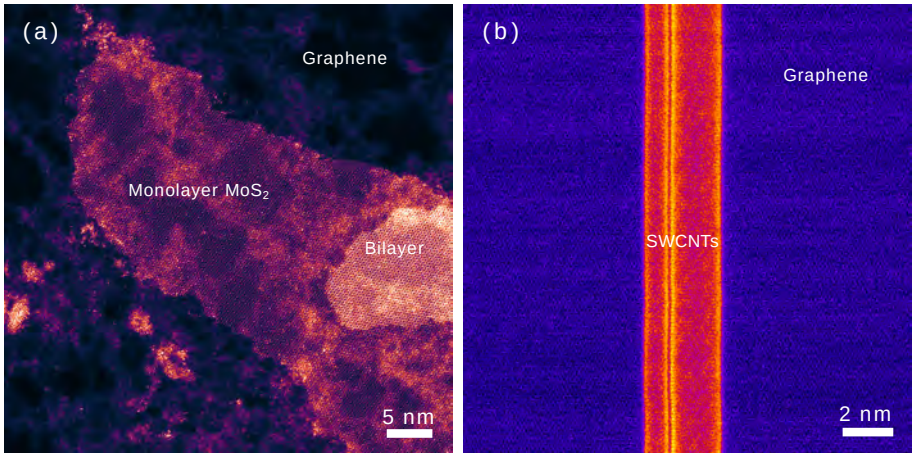

Figure 1.8: The STEM-ADF images of multidimensional heterostructures: (a) graphene-MoS_2 (2D-2D) and (b) graphene-SWCNTs (2D-1D) heterostructures.

1.2 Modification of ultrathin materials

Independent of consisting of stacked or individual molecules, low-dimensional materials are sensitive to atomic scale modifications e.g. a replacement of an atom in lattice, which hence allows us to chemically and physically manipulate their properties. The modified materials exhibit novel properties and functionalities that are not present in their pristine equivalents and can thus be used for particular applications. There are various ways to modify the properties of materials e.g. electrical biasing, high temperature, gaseous environments, liquid cells and particle irradiation. For example, graphene and CNTs can be chemically modified by implantation of heteroatoms (B, N or Si etc.) into the lattice [57, 16, 58, 13], incorporation of atoms or molecules inside tubes [59] and adsorption of atoms or molecules on the surface [60]. Many studies have shown structural evolution [25, 61], and defect and edge engineering [62, 63] of TMDs and their stacked systems under electron irradiation and at high temperatures. In this thesis, I will discuss such methods as ion irradiation and Joule-heating as tools to modify the covalent structure of the earlier mentioned low-dimensional materials.

1.2.1 Defects in materials

Both intrinsic and extrinsic defects may exist in materials. They can be categorized according to their dimensionality such as 0D (vacancies, adatoms, interstitial atoms and substitutional impurities), 1D (line, grain boundaries and edges) and 2D (folds, wrinkles, ripples and large pores). These defects affect the physical properties of materials. For example, grain boundaries in WS_2 behave as conducting channels [64] and creation of strained sulfur vacancies or inclusion of dopants in MoS_2 affect the local electronegativity and allow their use for catalysis [65, 66]. Thus, defects are useful to manipulate the properties of materials for particular applications. Intrinsic defects form spontaneously during material synthesis and separation and are generally not desired, for in that case their morphology and spatial distribution cannot be controlled. Defects can be introduced on purpose by exposing materials to electron irradiation, plasma or highly charged ions. The most common defects are point defects (such as mono- or di-vacancies). The mono- and di-vacancies refer to one and two adjacent atomic sites that are vacant, respectively. Fig. 1.9 depicts some, but not all, point defect configurations that are present in graphene and CNTs.

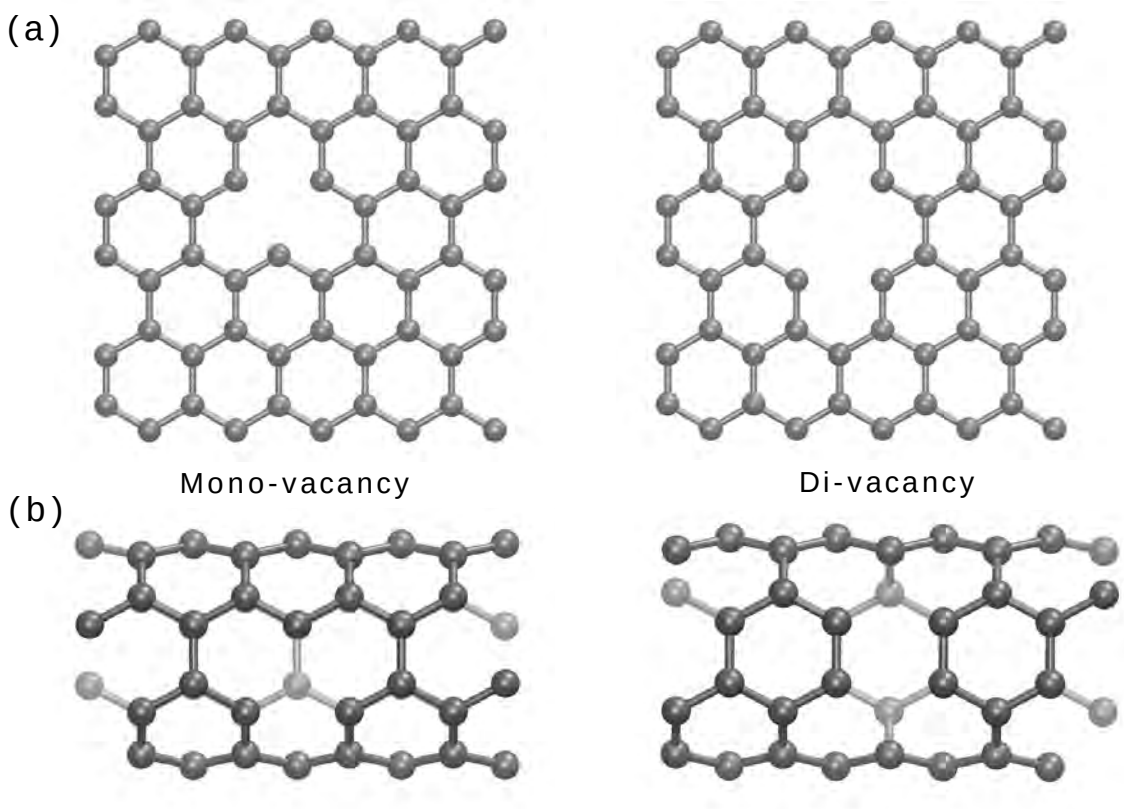

Figure 1.9: Atomic models of mono and di-vacancy in (a) graphene and (b) single-walled carbon nanotube lattice.

1.2.2 Ion irradiation

Ion irradiation is a widely used and a versatile tool to tailor the atomic structure and properties of materials. When ions pass through a specimen, they loose energy via collisions with electrons and nuclei in processes that can thereby produce defects. The nuclear energy loss due to interaction of ions and nuclei of atoms through elastic collisions is called nuclear stopping, whereas energy loss due to interaction with electrons through inelastic collisions is called electronic stopping. The amount and mechanism of the energy loss depends on the velocity and mass of the ion, and that of the target material [67]. The subsequent modifications are different for certain type of ions such as highly charged ions [18], swift heavy ions [68] and focused ion beams [69].

Highly charged ions (HCIs) refers to the ions with high ionized states (Q = up to +92). The high ionized states of atoms are attainable by removing a number of electrons from the outer electronic shells of the atom, leading to an increase in its potential energy. In this case, potential energy is a sum of ionization energies of all missing electrons and thus a function of the charging state, and it can reach up to several tens of keV [70] for Ar and Xe ions. Slow (1 eV/amu-10 keV/amu) highly charged ions can induce nanometer scale surface modifications in the materials resulting from deposition of potential energy of ions into the target system. Due to low velocities and high potential energy, the interaction leading to a rapid change in the charge distribution and in some cases, to covalent changes in the material [71]. For instance, in MoS_2, the impact of HCIs lead into the formation of nanometer size pores [18]. A high level of ionization can be achieved via electron beam traps (EBITs) or electron cyclotron resonance ion sources (ECRISs).

In plasma irradiation, the specimen is exposed to ions generated in different gaseous environments (e.g. $Ar/N_2/O_2$) by supplying energy to a neutral gas which leads to ionization through collisions between electrons and atoms or molecules in the gas. The typical ion energies are low (down to 20 eV). Therefore, the interaction between the ions and the target falls into the nuclear stopping regime. Typical plasma sources are direct-current (dc), radiofrequency (rf) and microwave generators.

Chapter 2

Methods

In this section, I will introduce techniques and tools which were used to carry out the experiments and characterize the materials. A dedicated scanning transmission electron microscopy (STEM) instrument with customized ultra-high vacuum setup was used for observing the structure of materials, their dynamics under external stimuli such as Joule-heating, plasma and HCI irradiation for the experiments discussed later. HCI irradiation experiments were performed at TU Vienna.

2.1 Scanning transmission electron microscopy

Microscope is a tool that allows us to examine structural details of materials by forming magnified images. The very first microscope, developed in 17th century, used visible light passed through lenses, to form an image of the object [72]. Initially, the limiting factor for resolution was the quality of convex lenses, which was later improved by using more than one lens to create a compound microscope. However, the resolution of a light microscope is also limited by the wavelength of visible light and hence it is not possible to resolve objects that are smaller than a few hundred nanometers. Later in the 20th century, it was understood that accelerated electrons that can have a wavelength much shorter than the size of an atom or typical interatomic distances in solids, could hence used to resolve atoms. For example, at an acceleration voltage V_0 of 100 kV, electrons with charge e and rest mass m_0 have a relativistic wavelength

$$\lambda = \frac{h}{\sqrt{\left(\frac{eV_0}{c}\right)^2 + 2m_0eV_0}} \simeq 3.7 \text{ pm},$$

where h is a Planck constant (6.63×10^{-34} Js) and c is the speed of light (3×10^{8} ms^{-1}).

In 1931, Ernst Ruska and Max Knoll developed the first transmission electron microscope (TEM) with which they produced images at a resolution higher than a light microscope by replacing the light source with an electron source, optical lenses with magnetic lens and the projection screen with a fluorescent screen [73]. Shortly after that, scanning transmission electron microscope (STEM) was invented by Baron Manfred [74]. In (S)TEM, the resolution is limited by spherical (C_s) and chromatic (C_c) aberrations originated from electron lenses which was first described by Otto Scherzer [75]. Due to C_s, electrons away from the optical axis focus at higher strength than those near to the axis and produce an undefined focal point which leads to the blurred appearance of the object on the image plane. C_c originates from the energy difference of electrons that therefore are focused on different focal planes. In 1966, first breakthrough was achieved by Albert Crewe by developing a cold field-emission gun (CFEG) with which it was possible to form small electron probe with high currents and extremely small electron energy spread of $\sim$0.3 eV, that allowed to obtain high-resolution images with high signal-to-noise ratio [76]. The next breakthrough came as aberration corrector for TEM invented by Haider and Zach [77, 78] and Ondrej Krivanek and co-workers achieved the spherical aberration correction in dedicated STEM instrument [79, 80, 81]. This not only allowed atomic resolution imaging but also made it possible to image the sample at lower voltages minimizing the knock-on damage to samples of lighter atoms.

The basic principle of electron microscope is the collection of electrons scattered from the sample due to electron-matter interaction and using them to form a magnified image. When an electron passes through a sample, it interacts with the nuclei and the electron cloud of atoms in the specimen, which lead to elastic and inelastic scattering, respectively. Fig. 2.1 illustrates all possible processes in electron-matter interaction. In conventional TEM, a nearly parallel electron beam formed by the lens system passes through the sample and transmitted electrons are collected on a fluorescent screen [82]. In contrast, in STEM, a sharply focused electron beam scans pixel-by-pixel over the sample and elastically scattered electrons are collected by annular dark field (ADF) detectors to form ADF images which exhibit contrast dependent on the atomic number of the target atom (Z-contrast), which is easily interpretable (see section 2.1.1). The inelastically scattered electrons can be used for chemical and elemental analysis of specimen through spectroscopic techniques (see section 2.1.2).

In work leading to this thesis, I used a dedicated STEM instrument Nion UltraSTEM 100 installed in Vienna in 2013. An image of the instrument marked with all main components and a simplified schematic of the microscope are shown in Fig. 2.2. The instrument is equipped with a CFEG as

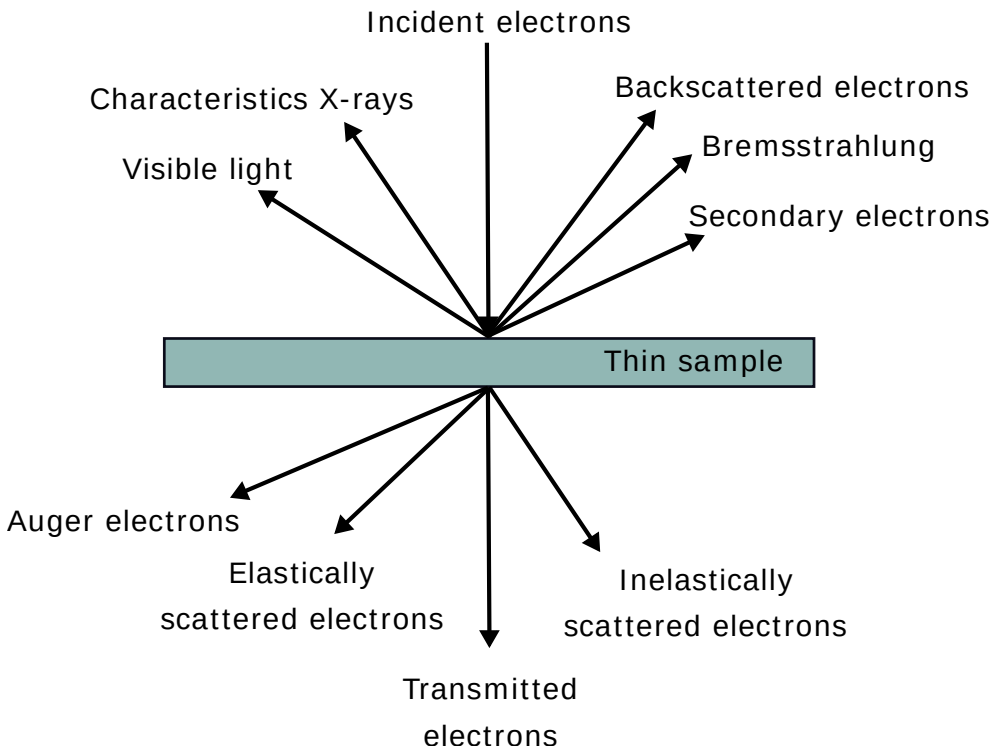

Figure 2.1: A schematic illustrates the different processes and variety of signals produced by the interaction of an energetic electron beam with a thin sample.

the electron source, with a typical electron energy spread of 0.3 eV. To minimize contamination and extending the life of the electron gun, the microscope operates in ultra-high vacuum (UHV). The pressure at electron gun is below $\sim 10^{-11}$ mbar. The microscope has an aberration corrector which corrects the aberrations up to the fifth order, and is physically located after the condenser assembly and before the sample and scan coils. The base pressure at sample is in normal operation conditions below $\sim 10^{-9}$ mbar range which is two orders of magnitude lower than in a typical (S)TEM. There are medium-angle ADF (MAADF) and high-angle ADF (HAADF) detectors and a charge-coupled device (CCD) camera which is used for shadow images (ronchigram) employed mainly for tuning and alignment of the microscope. For spectroscopy, the instrument is quipped with Gatan EEL spectrometer and an Andor iXon Ultra 897 electron-multiplying charge-coupled (EMCCD) camera. A detailed description of the instrument can be found in Ref. [83].

The microscope in Vienna is further equipped with a customized objective and a sample stage [84] connected to an ultra-vacuum ($\sim 10^{-9}$ mbar) system which allows sample transfer between the microscope and other stages of home-built UHV sample preparation, manipulation and transfer system (details in section 2.1.5).

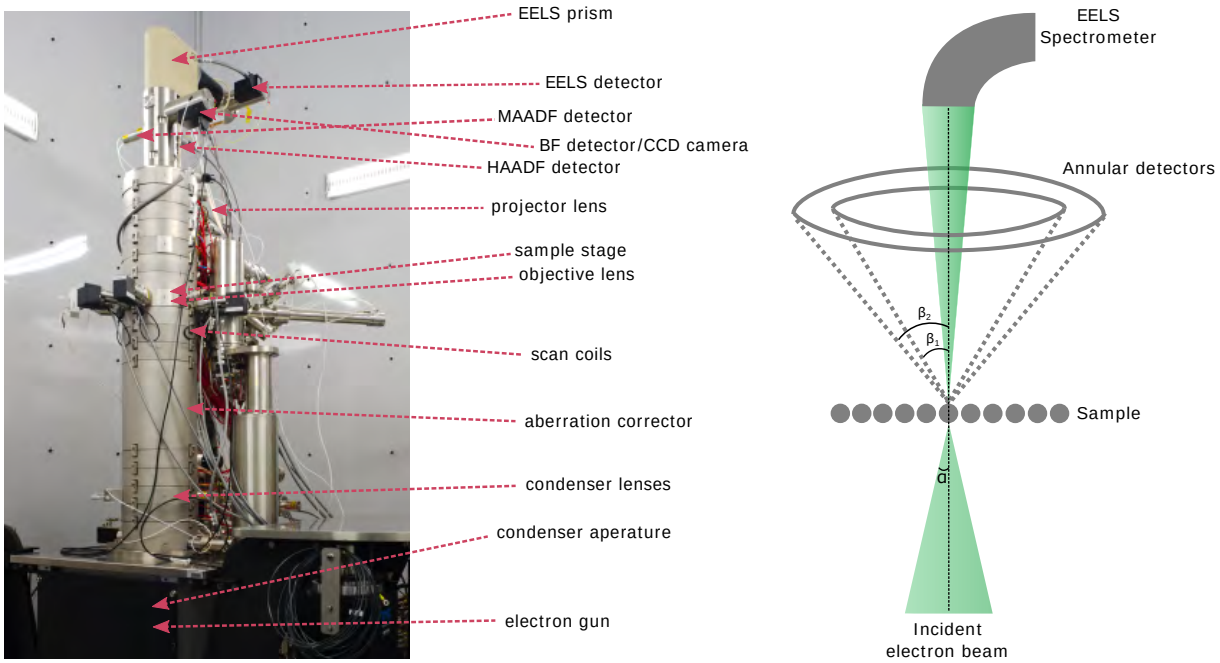

Figure 2.2: Photograph of the Nion UltraSTEM 100 instrument (left) labeled with all main components and a simplified schematic of STEM (right).

2.1.1 ADF imaging

Annular detectors are ring-shaped and collect electrons that have elastically scattered from the specimen as shown in a schematic (Fig. 2.2(right)). The circular hole in the center of the detector passes transmitted electrons including inelastically scattered electrons through for use in electron energy loss spectroscopy. They differ in annular range as the HAADF detector in the microscope used in this thesis has a detection range (in solid angle) of 80-300 mrad, whereas the MAADF detector's range is 60-200 mrad. Upon interaction of the electron beam with a sample, some of the electrons scatter from the nuclear electrostatic potential of the atoms and deviate from their original trajectories. Thus the process can be considered to be Rutherford scattering especially at high angles and the scattering angle of the electrons depends on strength of the electrostatic interaction. The contrast of an atom is thus related to the atomic number as $I \sim Z^{1.7}$ in HAADF mode [85]. In contrast, low angle scattering is due to Bragg diffraction. In principle, HAADF annular range can be used to collect scattered electrons from every sample. However, high-angle scattering is less likely for light elements which leads to a lower signal. Therefore, MAADF is better suitable for materials consisting of light elements. An example of MAADF imaging is present in Fig. 2.3. Fig. 2.3(a) shows a raw ADF image of the atomically resolved defected graphene lattice with Si heteroatoms. In Fig. 2.3(b), a Gaussian blur filter was applied to reduce the noise and in Fig. 2.3(c) shows a filtered image with color scale to enhance the contrast. The

scattering intensity is recorded for each probe position. Therefore, atomic sites in specimen can be detected as intensity peaks, and low intensity corresponds to vacuum i.e. no specimen. As in images, Si atom has significantly higher intensity than carbon atoms which can also be seen in intensity profile shown in Fig. 2.3(d).

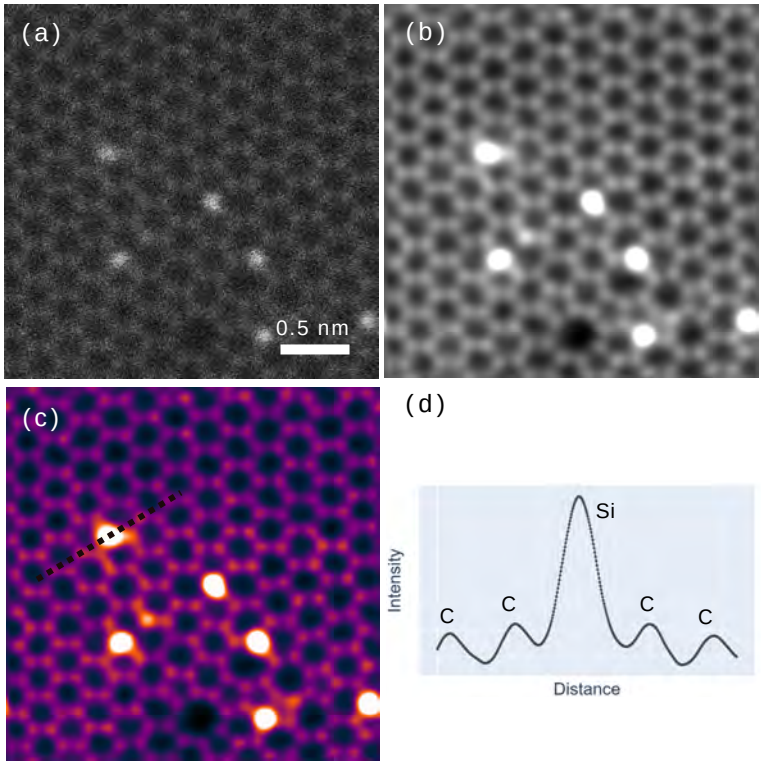

Figure 2.3: STEM-ADF images of graphene lattice with heteroatoms. (a) Raw image of the graphene lattice taken with MAADF. Some Si (bright) atoms are seen in lattice which can be easily identified based on their intensity. (b) Gaussian filtered image of panel (a) with 3-pixel radius. (c) Same as (b) with color scale to enhance the visibility of atoms. (d) Intensity profile along the line drawn in panel (c).

2.1.2 Electron energy loss spectroscopy

Electron energy loss spectroscopy (EELS) is an analytical technique that provides quantitative information of elemental and chemical composition in materials. As discussed above, when electrons pass through the sample, this leads to elastic and inelastic scattering. Elastically scattered electrons form images through interaction of incoming electrons with atomic nuclei. Whereas, when incoming electrons interact with the atomic electrons, a significant fraction of their momentum can be transferred in inelastic collisions. Inelastic scattering includes phonon and plasmon excitations, inner shell ionization and inter/intra-band transitions. By measuring the energy loss

with an electron spectrometer, a range of information can be obtained from the sample. For example, inner-shell ionizations are unique for each element and provide a fingerprint for their identification. This technique can also be used for measuring chemical bonding, band gaps and surface properties.

Inelastically scattered electrons scatter to relatively small angles (5-100 mrad) in comparison to elastically scattered electrons and are therefore not disturbed by the annular imaging detectors [86]. In practice, due to the need of high-energy electron beam, EELS can be combined with (S)TEM. As shown in Fig. 2.2, a STEM column is connected to an EELS spectrometer. In spectrometer, the transmitted and scattered electrons pass through a magnetic prism which disperses them based on their kinetic energies. As the electrons pass through homogeneous magnetic field $\vec{B}$ perpendicular to their momentum $m_e * v$, they bend in a circular path with a radius r due to Lorentz force. The radius of path is given by $r = \gamma mv/eB$ where e is electron charge and γ a relativistic factor. Because the radius depends on the energy of the particles, the distribution of energies can be obtained when the resulting spectrum is recorded. The first peak at 0 eV (zero-loss peak) represents the elastically scattered/transmitted electrons. The low-loss region at $<$50 eV contains information about band gaps, surface plasmons and phonons. The high energy losses at core-loss region ($>$50 eV) feature ionization edges. These edges are formed due to excitation of inner-shell electrons by beam electrons. For example, Fig. 2.4 shows a EEL spectrum with the C-K edge. An EEL spectrum is taken by localizing the electron beam at a specific position thus provides the information from corresponding site in sample. Additionally, there is possibility to acquire spectrum from each pixel in an image, known as spectrum imaging. This allows us to obtain large set of information from sample at each data point.

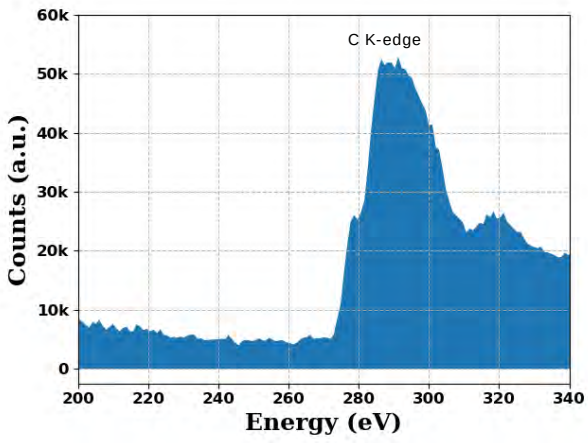

Figure 2.4: Core-loss EEL point spectrum taken at an atom position. The spectrum is background substracted and the presence of C K-edge at 284 eV identifies the atom as carbon atom.

2.1.3 Graphene as an electron transparent support

The background signal and noise due to sample support, thermal vibrations, charging and instability under the electron beam hinder the best possible resolution of the sample. The ideal sample support should contribute minimum background noise, be thin that electrons can pass through, and be stable under the electron beam. As the thinnest possible structure that consists of light carbon atoms, graphene is not only highly transparent to electrons but also resilient against knock-on damage, thus rendering it an appealing support for suspending TEM samples [87]. Indeed, graphene has been used as a sample support to study the structure of metal particles [88] and biological samples [89, 90]. It can also be used as a template for suspended nanotubes which otherwise vibrate and hinders atomic imaging [51]. Additionally, graphene's ability to sustain high electric current and high temperatures enable its use as a "conducting hot-plate" for *in situ* TEM experiments [91, 92].

2.1.4 *In situ* Joule-heating measurements

Joule heating is a form of resistive heating and refers to applying electric field across the sample. It can be used to provide insight into structural behavior of materials at elevated temperatures when carried out during microscopy. A voltage difference between two points of a conductor create electric field which leads to the acceleration of charge carriers. The energetic charge-carriers tend to scatter in random directions by colliding with atomic ions in the material giving rise to thermal energy. This in turn leads to a temperature increase in the lattice and can significantly impact the structure and physical properties of the material.

To be able to apply voltage/current through the sample in the microscope, we fabricated electron microscopy compatible devices with different device structures and used a customized electrical cartridge holder provided by Nion Inc. Devices were mounted on the holder shown in Fig. 2.5 used to transfer the samples inside the microscope. Two-probe measurements were carried out using a Keithley 2614B source meter with a high stability current source. Different device geometries used in experiments presented in this thesis are shown in Fig. 2.6.

The first device was fabricated on to SiN chips with a hole size of 3 μm (more details in section 2.2.2) on which graphene was suspended with two Au electrodes. This simple device structure proved to work for low-resolution experiments at comparatively low temperatures, but was not efficient for atomic-scale resolution due to vibrations and sustainability at high temperatures.

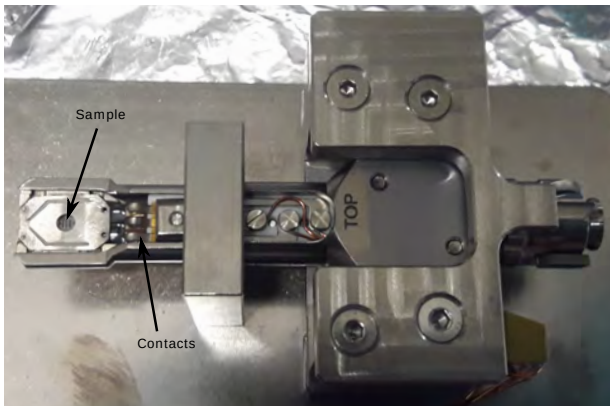

Figure 2.5: A photograph of electric cartridge holder used for electrical measurements inside microscope.

The chips broke at temperatures higher than 1200°C. Later, we used customized chips provided by Protochips Inc. for better stability that allowed atomic resolution imaging. In two-probe measurements, the Keithley source meter and a customized software was used to apply voltage sweeps to the sample while image sequences were recorded with the microscope.

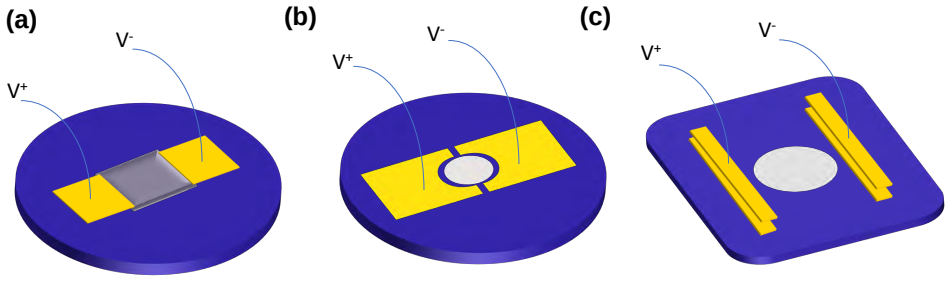

Figure 2.6: Different device structures used for electrical measurements. (a) SiN substrate with two Au electrodes (b) SiN substrate with two Au electrodes surrounding the hole (c) Protochip, material is sandwiched between electrodes by placing two Au electrodes on existing ones. $I-V$ characteristics are observed by applying the voltage between two electrodes.

2.1.5 Ultra-high vacuum setup

The Nion UltraSTEM100 instrument installed in Vienna has been customized with in-house built vacuum setup which allows sample preparation and transfer in ultra-high vacuum ($\sim 10^{-9}$ mbar). The microscope was installed as shown in Fig. 2.2(left) with the standard sample insertion method

consisting of magazine with five slots for sample holders, shown in Fig. 2.7(a). To prevent any vacuum contamination and to remove water from the sample surfaces, the magazine with sample holder is baked at 180°C a minimum of 6 hrs at baking station (Fig. 2.7(c)). For instance electrical samples can only be inserted to the microscope from the magazine. However, customized samples without electrical contacts can also be inserted from an interconnected vacuum setup via a customized sample arm that is a part of the modified Nion microscope in Vienna (Fig. 2.8(a)). For this purpose, different sample holders ("pucks") were designed. They can be inserted into a vacuum "car" that can be steered through the vacuum system with a pair of magnets coupled outside. Photographs are shown in Fig. 2.7(d-f). Additionally, the system is equipped with a high power diode laser (tunable up to 6 W) of 445 nm wavelength from Laserstack GmbH, pointing towards the sample area in microscope through a viewport, which allows us to clean the samples via laser annealing inside the microscope. Further, the system consists plasma source and an evaporation chamber [93]. In this thesis, samples were transferred with vacuum cars between the microscope and a manipulation chamber, where modifications were inflicted with low-energy ions. Photographs of customized microscope setup and ultra-vacuum set-up consisting manipulation chamber and plasma source are shown in Fig. 2.8.

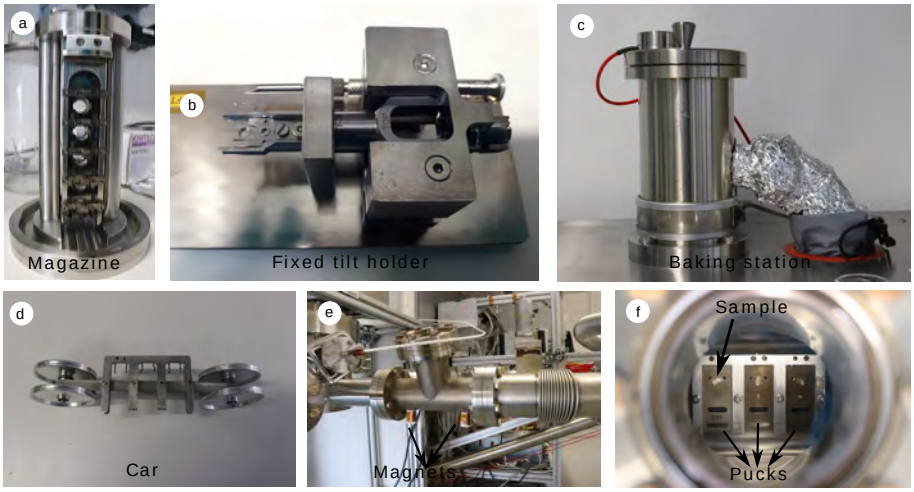

Figure 2.7: Photographs of sample holders. (a) Magazine holder with five slots for cartridges (b) A cartridge holder containing the sample goes into the magazine. (c) Baking station (d) Car, a customized sample holder with three slots for pucks that can travel through vacuum line (e) Magnets for driving the car (f) Puck, a customized sample holder containing a sample.

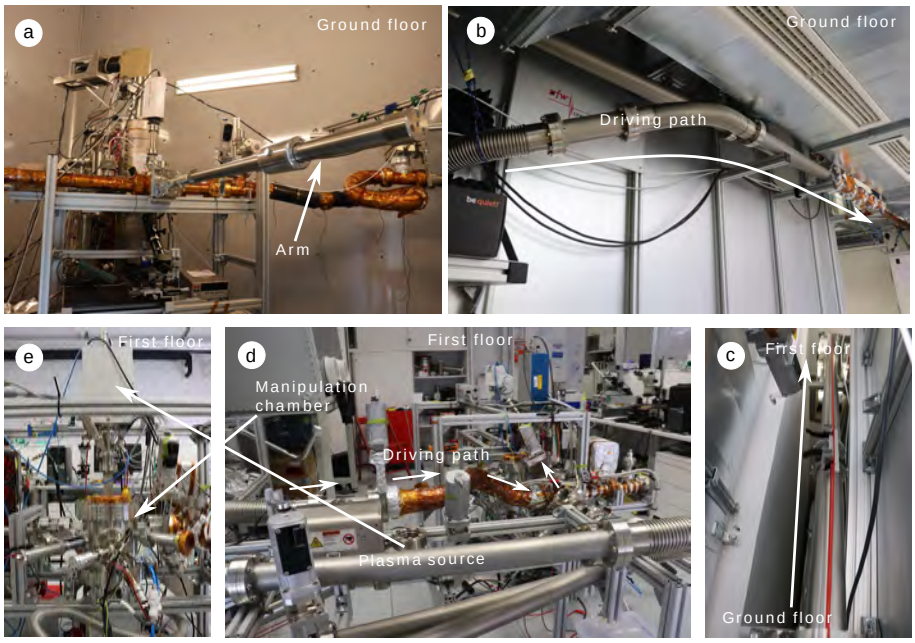

Figure 2.8: Photographs of customized STEM and ultra-high vacuum set-up. (a) Customized Nion UltraSTEM100 instrument. An arm is marked with white arrow, it allows us to pick the puck and insert into objective area and stage. (b-d) Driving path for car from microscope to manipulation chamber (e) Manipulation chamber and plasma source.

2.2 Sample preparation

In this section, I will describe methods for sample preparation and device fabrication. All samples are either individual or heterostructure systems consisting of graphene, CNTs and MoS_2 materials, and graphene is primarily used as a support or material to be investigated. The materials used here were either commercially available (graphene) or obtained from collaborators (MoS_2 and SWCNTs). Therefore, I will not describe the synthesis methods for individual materials.

2.2.1 Preparation of 2D-2D/2D-1D heterostructures systems

Two-dimensional materials (graphene, TMDs etc.) can be usually obtained from micro-cleavage of layered bulk crystals using scotch-tape [6] or chemical vapor deposition method [94, 95]. For example, graphene can be obtained with micro-cleavage of graphite crystal. Additionally, they can be obtained by liquid exfoliation methods [96] for large scale production. Carbon nanotubes can be synthesized by high-energy processing techniques such as carbon-arc discharge, laser ablation and CVD [97]. Van der Waals heterostructure systems can also be fabricated by micro-cleaved layers or chemical vapor deposition (CVD) method. A desired stack of materials can be achieved

by transferring micro-cleaved isolated 2D sheets on top of each other in repetitive manner or grow through CVD processes [8]. The process of transferring layers one-by-one is straightforward and simple, and yet it is laborious and time consuming. However, CVD method is one-step process which is fast and reliable for commercialization of these systems.

Wet transfer method for graphene-MoS_2

Materials are synthesized either on Si substrate (in case of CVD grown MoS_2 or exfoliated graphene) or on metallic foil (in case of CVD grown graphene). For STEM investigations, we need to transfer them on an electron transparent support. The support used in this experiment was a 3 mm 200 mesh[2] (a mesh size refers to the number of grid bars per inch) TEM gold grid coated with a perforated amorphous carbon foil. For graphene-MoS_2 heterostructure systems, CVD grown MoS_2 on Si substrate and commercially available CVD graphene on TEM grids were used. To begin with, monolayer MoS_2 flakes were found on Si substrate under an optical microscope based on their transmittance and thus, thickness. Next, a TEM grid with pre-transferred graphene is placed on the desired area and fixed with a micro-manipulator. A few droplets of isopropyl alcohol (IPA) is used it to adhere on the Si substrate through drying. Next, few drops of KOH were put at grid edges to etch away SiO_2 and to detach the grid from the substrate. Finally, the grid is rinsed in IPA and water to get rid of acid and then air dried, resulting in MoS_2 monolayer flakes on graphene grid. A schematic shown in Fig. 2.9 depicts the each step of the method.

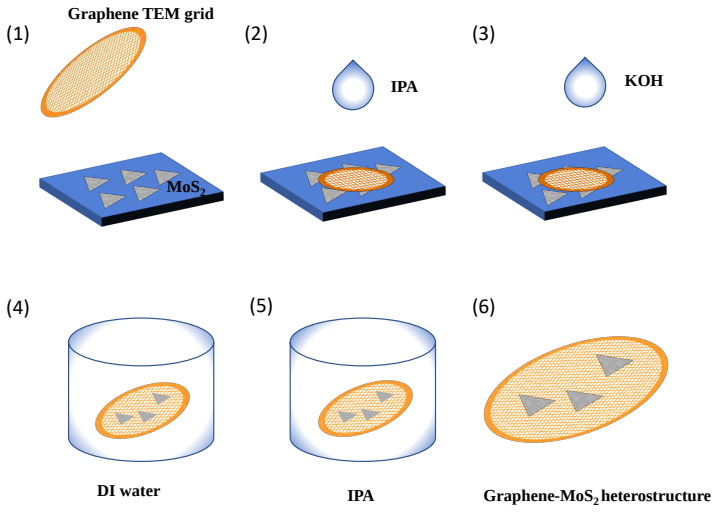

Figure 2.9: Step-by-step process for wet transfer method of monolayer MoS_2 on graphene.

Dry deposition of carbon nanotubes on graphene

For graphene-SWCNTs heterostructure system, CVD grown graphene and floating catalysts SWCNTs were used. Nanotubes were synthesized in a floating catalyst using ferrocene and ethanol as catalyst precursors and carbon source [98]. First, commercially available Graphenea Easy Transfer graphene delivered on a poly (methyl methacrylate) (PMMA) support was transferred on silicon nitride (SiN) TEM grids. The PMMA was removed by thermal annealing at 400°C in Ar/H_2 environment. Finally, SWCNTs were directly deposited on the grid via thermophoresis method [99]. In this method, CVD reactors are connected with plate-to-plate thermophoretic precipitator (TPs). The TP consists of two aluminum plates separated by a sheet of teflon with a rectangular channel which allows gas flow between the plates. The top plate is maintained at high (100°C) temperature and the bottom part supporting also the sample and isolated from the top by the teflon sheet, maintained at ambient temperature. The steep temperature gradient in the gas flow channel leads to an uneven momentum transfer from the gas molecules to aerosolized SWCNTs, which thus drift towards the lower temperature plate. This results to a fraction of the reactor exhaust to become deposited on the TEM grid. This method allows the direct deposition of SWCNTs aerosols on the TEM substrates and the density of the deposited nanotube film depends on the deposition time. A schematic of thermophoresis deposition method is shown in Fig. 2.10.

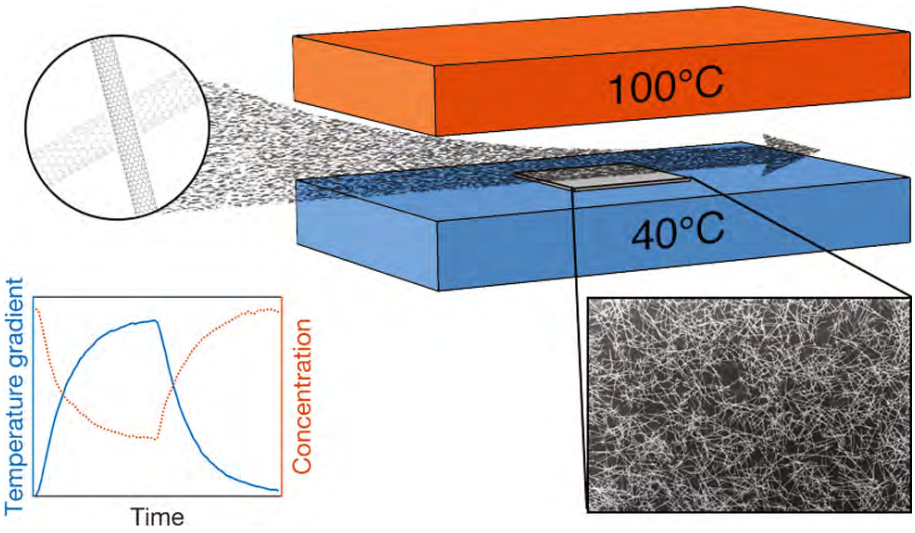

Figure 2.10: A schematic illustrating the thermophoresis deposition of SWCNTs adapted with permission from Ref. [99].

2.2.2 Device fabrication for electrical measurements

For *in situ* electrical experiments, we fabricated various TEM compatible device structures. First device structure was fabricated on a round Si substrate (diameter 3 mm) which has a 0.45 x 0.45 mm^2 silicon nitride window in the middle. We masked the window with stainless steel mask and evaporated two Au electrodes using thermal evaporation. This devices was sustainable until 1000°C. For higher temperatures, we used electrical Protochips (from Protochips Inc.) chips as sample support. The step-by-step fabrication process of each device is discussed in respective results section.

2.3 Ion Irradiation

2.3.1 Low-energy ion irradiation using a plasma source

As mentioned in section 2.1.5, the microwave hybrid plasma source from SPECS GmbH is attached to the UHV transfer setup. Different gaseous ($Ar/N_2/O_2$ etc.) plasma can be produced in the system by leaking the gases into the chamber through a leakvalve. The plasma pressure is defined by the leak and pumping rates and is usually in the order of $\sim 10^{-6}$ mbar. The plasma source [100] is a chamber of aluminum oxide in which plasma is created through microwave discharge induced by a magnetron. The system operates in two modes: atom mode or ion mode. In atom mode, mostly neutral atoms are produced and charged atoms are blocked by dielectric apertures. In contrast, in ion mode, mainly charged atoms are extracted from the plasma. They are obtainable by applying a negative potential to the extractor electrode and a positive potential to the second electrode. The negative potential extracts positively charged ions from the plasma and the positive potential accelerates them towards the specimen.

To define the total energy of the ions, it is important to mention that the atoms in the plasma already have an intrinsic kinetic energy of 25 eV due to the plasma sheath potential [101]. This potential is created because electrons containing higher thermal velocities than ions escape from the plasma and often collide with chamber walls. Once the electrons are depleted, a region is formed with positive ions and neutral atoms near chamber walls, known as the potential sheath. This charge imbalance creates a plasma potential (acceleration potential) with respect to the grounded walls of the chamber which needs to be added to the plasma potential.

For the experiments presented in this thesis, we used Ar plasma with a total energy of 50 eV

(sheath potential + 25 eV acceleration) to irradiate the specimen in order to create point defects in graphene and carbon nanotubes. According to a theoretical models, the maximum probability to create point defects in graphene is at 50 eV without creating a large amount of complex defects configurations [102]. Since impingement of ions on hydrocarbon contamination that is found on surface of graphene leads into dehydrogenation and chain-interlinking, we used here a high-power laser to elevate the sample temperature above the sublimation point (ca. 500°C) of such impurities. This had a significant effect on reducing the residual contamination.

2.3.2 Highly charged ion irradiation

Highly charged ions can be produced using electron beam ion traps (EBITs) or electron cyclotron resonance ion sources (ECRISs). Irradiation experiment presented in this thesis was performed at TU Vienna. HCI ions were created in an electron beam ion source (EBIS) commercially available from Dreebit GmBH Dresden. A schematic of an EBIS is shown in Fig. 2.11. This ion source allows us to produce highly charged ions of almost every element. Ion source consists of a source chamber, drift tubes, a Wien filter and an extraction system. The base pressure in the chamber is at 10^{-9} mbar and ion beam currents are of $>$100 fA and can reach up to $\sim$10 pA. A high intensity electron beam was generated inside the source chamber which ionizes the working gas (Ne-like Xenon in this case) and ions pass through magnets and three drift tubes. The drift tubes are at different extraction voltages confining the ions in the axial direction. Then ions pass through the extraction lenses, and a Wien filter is used to select a specific charge state by mass-to-charge ratio. The ion beam energy can be adjusted by an electrostatic deceleration lens system [103].

In our experiments, we used Xe^{+38} ions with a potential energy of 33 keV and a kinetic energy of 1.3 keV. Irradiation experiment was performed in ultrahigh vacuum (lower than 1 X 10^{-9} mbar). The samples were transported between the ion irradiation setup and the STEM instrument in air.

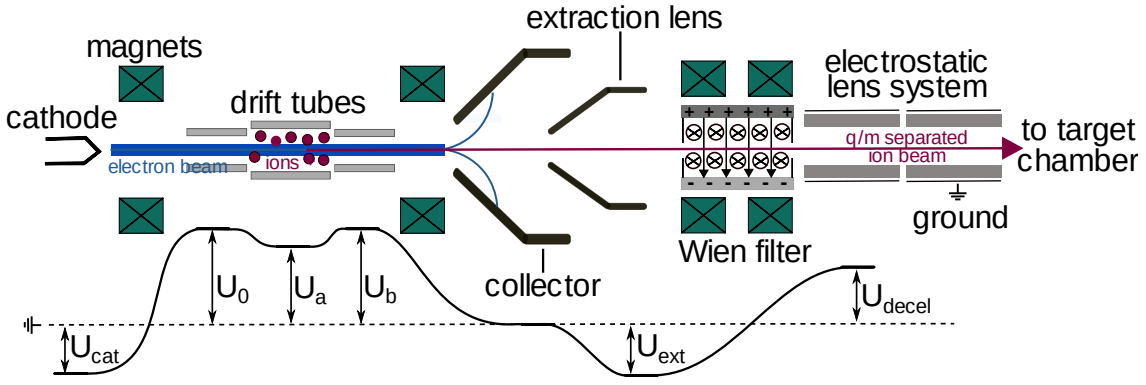

Figure 2.11: A schematic of highly charged ion source adapted with permission from Ref. [103].

Chapter 3

Results and Discussion

In this chapter, I will describe the experiments performed for this thesis and their results published in peer reviewed publications. Each publication is described in its own subsection.

3.1 Si heteroatom substitution into graphene-CNTs heterostructures via plasma irradiation

The content in this section corresponds to the results of the seventh entry in the list of publications [7].

In this experiment, we substitute Si atoms into both graphene and SWCNTs using low energy plasma irradiation. The main objective is to produce reactive sites (vacancy-type defects) in graphene and SWCNTs and to fill them with heteroatoms. A computational study by Tolvanen et al. [102] showed that vacancy formation is possible using low-energy (0.05-1 keV) range with Ar ion irradiation.

For graphene-SWCNTs heterostructure, commercially available CVD grown graphene was transferred onto silicon nitride supports, and SWCNTs grown via floating catalyst CVD were deposited onto it using the dry thermophoresis method (see section 2.2.1). The sample was transferred into the Nion UltraSTEM 100 microscope, where it was exposed to laser irradiation with 100 mW of laser power in the microscope column, resulting in clean interfaces. STEM images were acquired at an acceleration voltage of 60 kV. Fig. 3.1 shows STEM-MAADF images of the graphene-SWCNTs interfaces before and after cleaning. Overview images of pristine and cleaned tubes on graphene are shown in Fig. 3.1(a-b).

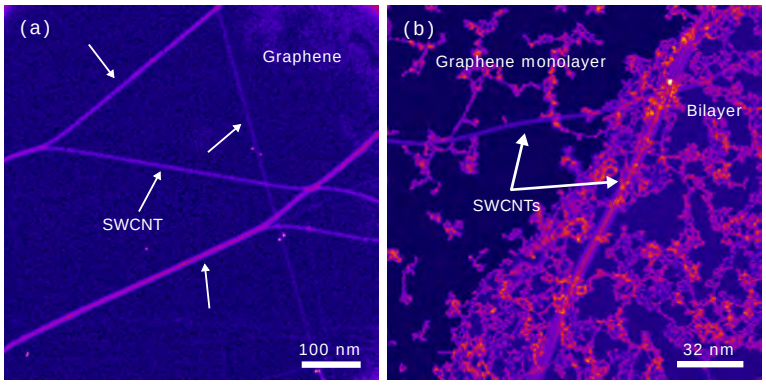

Figure 3.1: Overview STEM-MAADF images of pristine and laser-cleaned graphene-SWCNTs heterostructure. (a) Pristine sample, SWCNTs marked with white arrow on graphene (b) laser-cleaned SWCNTs on graphene, dark contrast represents the clean patches of graphene lattice.

Next, the cleaned samples were transported to the plasma irradiation chamber using the vacuum car system (see section 2.1.5) where they were exposed to Ar ion irradiation. The pressure in the chamber was maintained at $\sim 5{\times}10^{-6}$ mbar and the Ar plasma was ignited in a microcavity and accelerated to $\sim$ 50 eV of total energy, irradiating the sample with a dose of $\sim$ 1 ion/nm^2. To prevent contamination buildup during irradiation, the sample was simultaneously laser irradiated with laser power of 100 mW. Fig. 3.2(a) shows STEM-MAADF overview image of the sample after irradiation, illustrating the preservation of clean area, although patches of contamination pockets still present. These are likely to be highest chemical reactivity sites with a greater extent of lattice disorder. An atomically resolved view of irradiated SWCNTs on graphene is shown in Fig. 3.2(b), where we can see some heavy atoms (with a high intensity) captures in the carbon lattices marked with white arrows. To identify their elemental composition, EELS was used. In particular, when analyzing atoms capture in SWCNTs, we chose to study sample areas where tubes were suspended over holes breached in graphene. Fig. 3.2(b) shows the atomic structure of two suspended SWCNTs in vacuum with several covalently bound heteroatoms incorporated into the lattice. The EEL spectra/spectrum images were recorded with the Andor iXon 897 electron-multiplying camera and spectrometer operated at energy dispersion of 0.5 eV/px. Fig. 3.2(e) shows the background subtracted spectrum recorded from the atom highlighted with white circle in Fig. 3.2(c), revealing based on core-loss L-edge and onset at 99 eV the atom as 4-coordinated Si [16, 104]. The spatial distribution of atoms was recorded in a spectrum image from each probe position and by mapping the Si L-edge intensity ($\sim$ 99-200 eV) shown in Fig. 3.2(d).

Si substitution is explained by the fact that reactive sites (mono- and di-vacancies) are created with the Ar^+ irradiation and subsequently filled with adatoms that are released by thermal energy

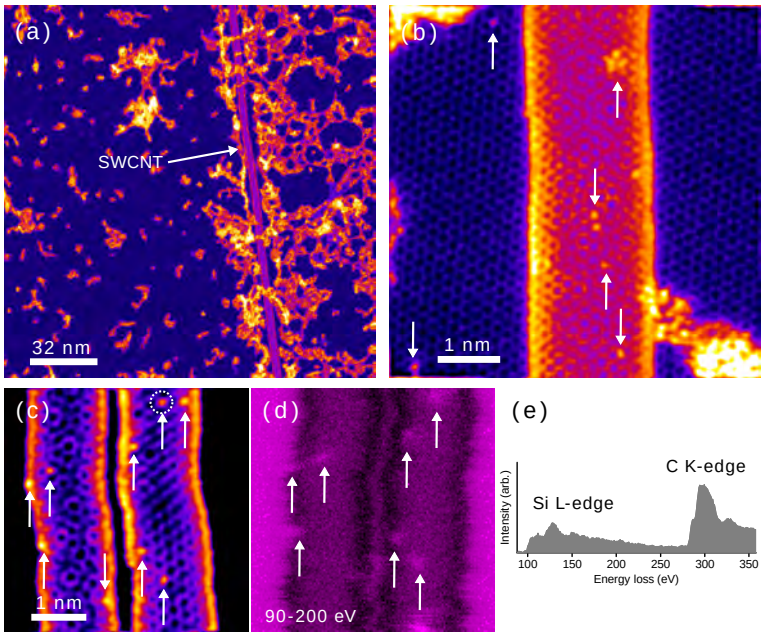

Figure 3.2: STEM-MAADF images of Ar plasma irradiated heterostructures. (a) Overview of plasma-irradiated sample (b) Atomically resolved image of irradiated interface, arrows mark the heteroatoms presence after plasma irradiation. (c) SWCNTs in vacuum containing Si heteroatoms in lattice, marked with white arrows (d) Mapped Si intensity in the range of 99-200 eV energy (128 px x 128 px), and (e) energy loss spectrum acquired from the atom highlighted with a circle in (c), consistent with four-coordinated Si. From Ref. [105] Copyright 2019 Authors.

provided by the laser irradiation. However, some vacancies in graphene remain unoccupied and reconstruct themselves into complex defects. It is known that Si atoms can be found in particular configurations with either 3 or 4 carbon neighbors [16] taking sites in mono- and di-vacancies, respectively. Since Si is present in large quantities in the amorphous contamination found on graphene, we expected some of the Si atoms to become trapped in the defects and indeed, both 3-fold and 4-fold were present in our experiments (Fig. 3.3). We observed the same configurations also in SWCNTs, with 63% being Si-C_3 and 37% Si-C_4 of the 61 Si sites analyzed (51 identifiable sites) in 31 separate tubes. These observations are also well in agreement with the predicted number of produced single and double vacancies on similar energies as we used [102]. Fig. 3.4 shows the STEM-MAADF images of Si-C_3 and Si-C_4 configurations in SWCNTs. In total, a surface area of 1200 nm^2 was analyzed with an areal density of $\sim$0.05 nm^{-2}. In graphene, total surface analyzed in atomic resolution was 1365 nm^2 and contained a total of 210 Si atoms. This corresponds to approximately three times higher areal density of $\sim$0.15 nm^{-2}. This is particularly interesting in that less energy is required to displace C atom in SWCNTs than graphene [106]. One confounding factor is that Si impurities that are never observed in SWCNTs are commonly

found in graphene [104, 107], but since their density is orders of magnitudes lower than what was observed here, this factor alone does not explain the large difference observed.

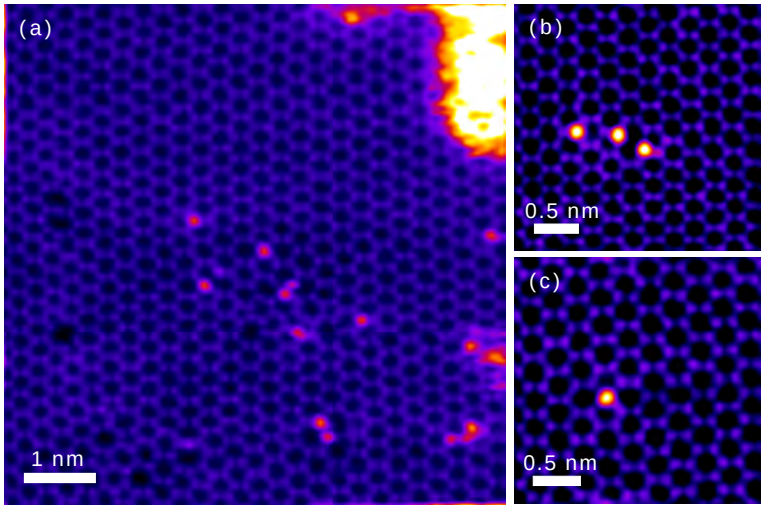

Figure 3.3: Atomically resolved STEM-MAADF images of Si-substituted graphene lattice. (a) Overview image of irradiated graphene lattice with point defects and impurities. (b) three Si atoms in 3-coordinated configurations, and (c) Si atom in 4-coordinated configuration. From Ref. [105] Copyright 2019 Authors.

However, since to reach the vacancies in SWCNTs the Si atoms must to migrate over the graphene basal plane, they also have many more opportunities to reach vacancies in graphene. To study the migration rates we calculated the diffusion barriers (and binding energies) for Si adatoms on graphene and achiral SWCNTs. The calculations were based on density functional theory (DFT) with the projector-argumented wave method implemented in the GPAW package, which revealed that the migration barrier was 0.06 eV on graphene and significantly higher, in order of 0.1-0.4 eV on SWCNTs, thus allowing Si migration on graphene even at room temperature.

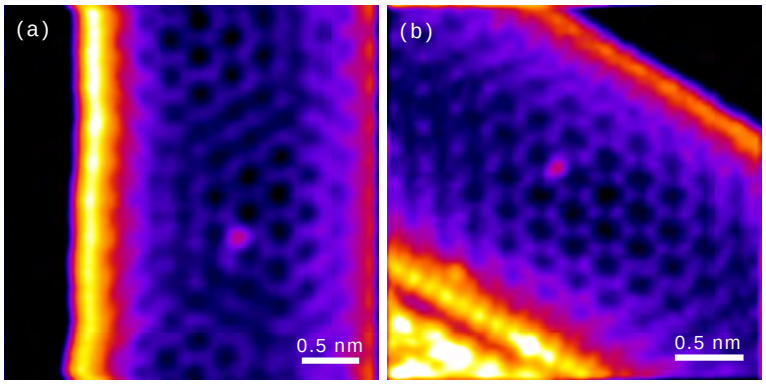

Figure 3.4: Atomically resolved STEM-MAADF images of Si heteroatom in SWCNTs lattice. (a) 3-coordinated and (b) 4-coordinated configurations of Si impurity in SWCNTs.

3.2 HCI irradiation of graphene-MoS_2 heterostructures

The content in this section corresponds to the third entry in the list of publications [3].

In this experiment, we irradiated graphene-MoS_2 heterostructures with highly charged Xe ions. Heterostructure samples were prepared by transferring CVD-grown MoS_2 flakes onto commercially available graphene TEM grids using a wet transfer method (as described in section 2.2.1). Samples were irradiated with 1.3 keV/amu Xe ions in a high charge state of 38 at a fluence of 1 x 10^8 ions/cm^2 at TU Wien, the ion beam facing towards both MoS_2 and graphene. Both pristine and irradiated samples were examined with the Nion UltraSTEM100 operated at an acceleration voltage of 60 kV. The microscopy images were recorded with a MAADF detector.

Fig. 3.5 shows overview and atomic scale images of pristine graphene-MoS_2 heterostructures. In these samples, MoS_2 coverage was over $\sim$ 50%. Fig. 3.5(a) shows an overview image of graphene-MoS_2 heterostructure, where white arrows are indicating the pockets of contamination. It is known that when two or more 2D materials come in contact, contamination between them is squeezed into pockets, leaving clean patches around [108]. The closeup view of MoS_2 on graphene are shown in Fig. 3.5(b-c). MoS_2 is an radiation sensitive material [109, 110, 111], as atoms can be displaced and sputter by gaining energy from high-energy electrons. For example, a defect site was created during imaging shown in Fig. 3.5(c). Samples were irradiated with HCI and later observed in microscope. Fig. 3.6(a) shows an overview image of irradiated graphene-MoS_2 heterostructure. After irradiation, in case of ion beam facing towards MoS_2, we observed several nanosize pores in MoS_2. Fig. 3.6(b) shows the close up view of irradiated sample, white circles indicate irradiation-induced pores and an atomic scale image of a pore marked with yellow circle in (a) is shown in Fig. 3.6(c). Interestingly, graphene lattice is unaffected by HCI irradiation.

In Fig. 3.7(a-c), a series of atomically resolved images is presented, revealing a nanometer-size pore only in the MoS_2 layer. In contrast, the graphene is still intact and lattice is clearly visible beneath the pore (Fig. 3.7(c)). This could be explained as the amount of potential energy was not sufficient to perforate graphene after passing through the MoS_2 layer. Alternatively, this could be due to the high conductivity of graphene, as it can provide electrons to neutralize ions at a relatively short time scale while charge transfer between the layers is too slow to resupply charges from graphene to MoS_2. Each pore in MoS_2 is considered to have been created by a single ion impact because of the low probability of double impacts ($< 10^{-7}$) at the used fluence (1 x 10^8 ions/cm^2). The average pore size corresponds to a sputtering yield of ions 340 at/ion. This results that the pores are formed with potential energy deposition not from direct knock-

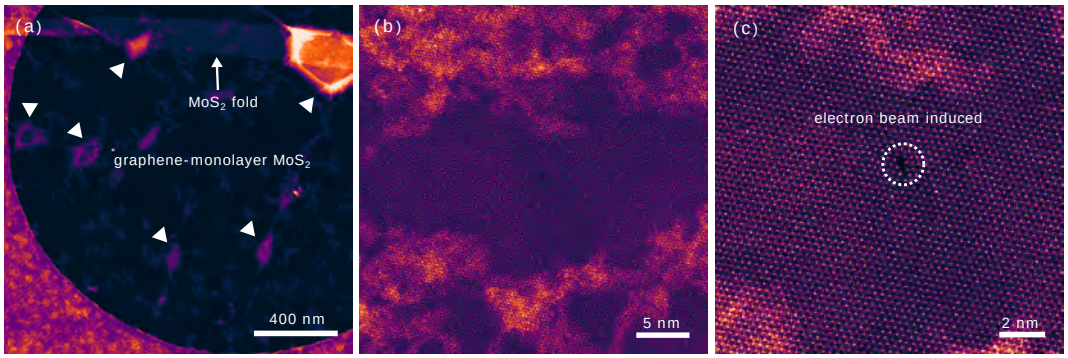

Figure 3.5: STEM-MAADF images of pristine graphene-MoS_2 heterostructures. (a) Overview image of monolayer MoS_2 on graphene, bright contrast represents the contamination pockets marked by white arrows. (b) Closeup view of MoS_2 lattice on graphene. (c) Atomically resolved lattice of MoS_2 on graphene; marked pore was formed by electron beam during imaging.

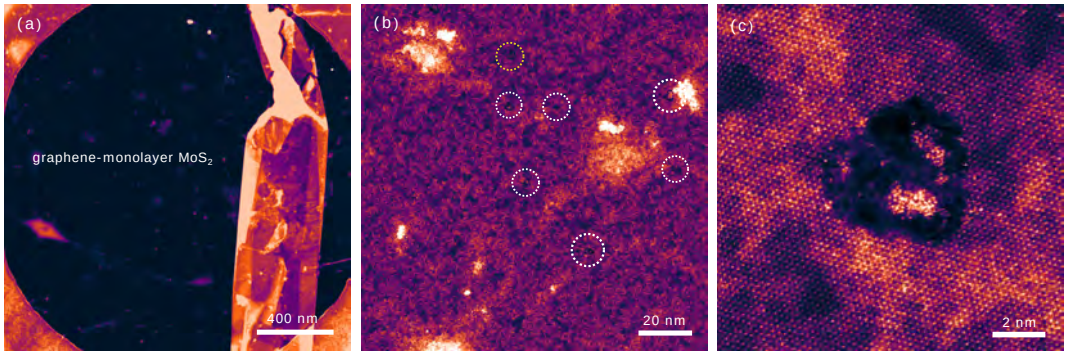

Figure 3.6: STEM-MAADF images of HCI irradiated graphene-monolayer MoS_2 heterostructures. (a) Overview image of the irradiated sample (b) Closeup image, white circles mark nanopores created by HCI irradiation (c) Atomically resolved image of a nanopore marked with yellow circle in (b).

on, as the yield would be much lower (2 at/ion) in that case [112]. For statistics, we analyzed a total of 68 pores in MoS_2 after irradiation from two different samples. We determined the area of pores and calculated the radius of pores considering them circular, although there also exist pores that do not follow this assumption. In our calculations we have excluded the pores created during imaging due to electron beam and present at grain boundaries [113]. Note that we were using electron beam energies at which damage cross sections are small and took care to minimize the e-beam exposure during imaging. A mean pore radius of $\sim$3.2 $\pm$ 1.0 nm was found for 1.3 keV/amu Xe^{+38} ions, which is in a good agreement with previous studies for irradiated freestanding monolayer MoS_2 [18]. The uncertainty value of 1.0 nm here represents one standard deviation of the Gaussian pore size distribution, whereas the error of the mean is much smaller 0.14 nm.

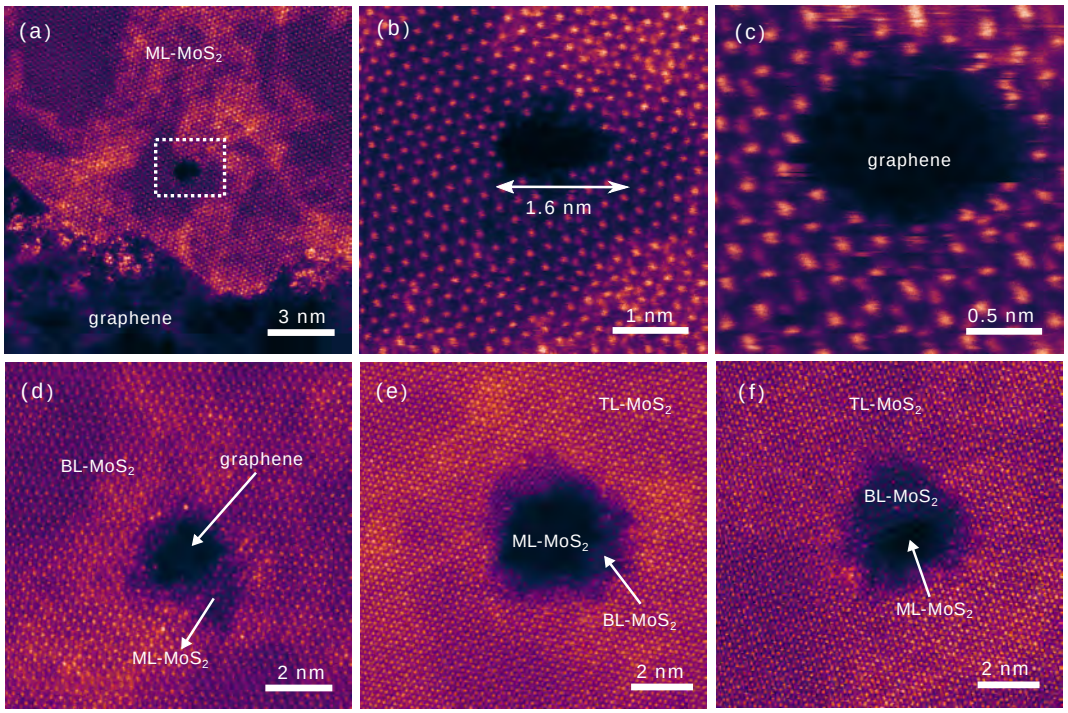

Figure 3.7: STEM-MAADF images of irradiated graphene-MoS_2 heterostructures. (a-c) Image series of a nanopore created in MoS_2 by HCI irradiation, while graphene lattice is intact and can be seen beneath the pore. (d) Irradiated bilayer MoS_2 on graphene, pore is created in both layers. (e) Irradiated trilayer MoS_2 on graphene, pore is created in upper two layers and monolayer MoS_2 lattice is seen beneath the pore. (f) Same as in (e), second layer is partially perforated. From Ref. [114] Copyright 2020 Authors.

Despite not being the main topic of the study, we also studied the perforation of multilayer MoS_2 on graphene. We observed that pore formation is possible in the first and the second layer with HCI irradiation. Fig. 3.7(d-f) shows the few cases of irradiated bilayer/trilayer MoS_2 on graphene. In case of the bilayer, both layers are perforated and the graphene lattice is visible beneath the pore, as in Fig. 3.7(a). However, in the trilayer configuration only the first two layers are perforated, whereas the third layer remains intact, and is visible in Fig. 3.7(e-f). These results indicate that the potential energy of 1.3 keV Xe^{+38} ions is deposited only in the first two layers of MoS_2, and as a consequence the remaining energy is not sufficient to perforate the third layer. This indicates that the number of modified layers can be controlled with energy and charge state of ions.

As a control experiment, the stacking order was reversed during irradiation so that graphene was facing the ion beam. Fig. 3.8 shows images of the irradiated sample. In this configuration, no structural changes are observed in neither graphene nor MoS_2.

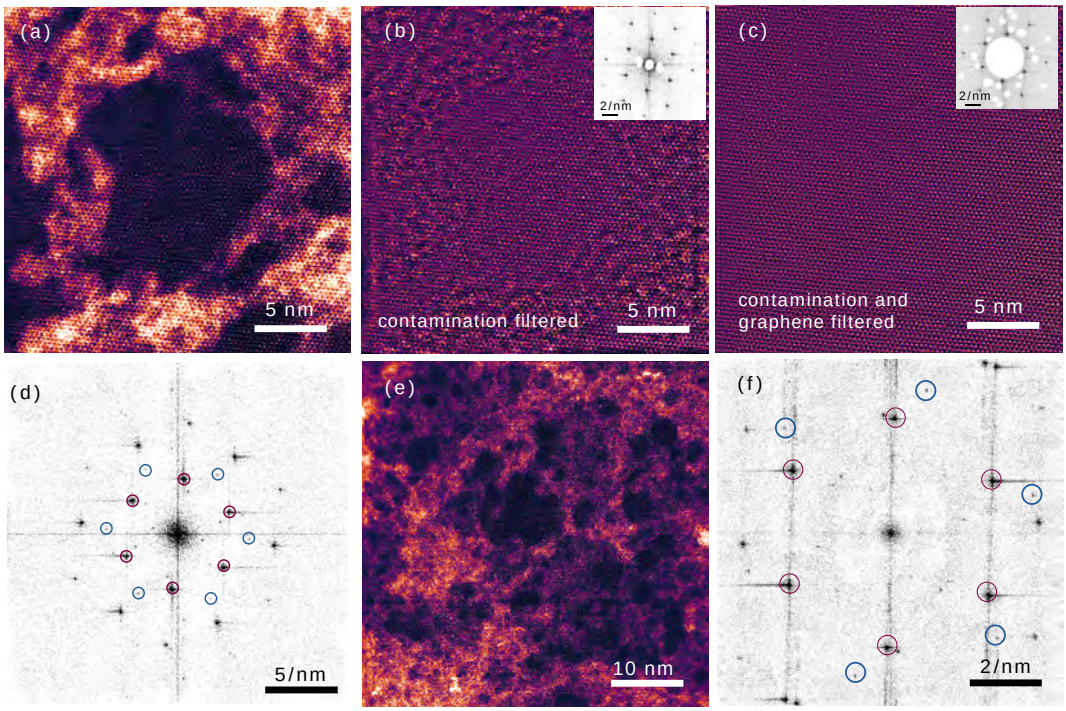

Figure 3.8: STEM-MAADF images of reverse stacked irradiated graphene-MoS_2 heterostructures. (a) Irradiated MoS_2-graphene heterostructures, no perforation in MoS_2. (b) Contamination filtered (a), FFT in inset residual spots are masked (c) Same as (b) but both contamination and graphene filtered, shows atomically resolved MoS_2 lattice. (d) FFT of (a), shows the spots of both graphene (red) and MoS_2 (blue) (e) large field of view image from the sample, (f) and its corresponding FFT. From Ref. [114] Copyright 2020 Authors.

The finding is consistent with earlier studies of HCI irradiated freestanding graphene [19]. Because the potential energy deposition is limited to the first layer, electronic excitations are largely created in graphene. However, due to the high carrier mobilities of graphene, charges are quickly resupplied and this prevents reordering of the atomic bonds [6, 19] and allows the MoS_2 layers beneath graphene to retain their structural integrity. Fig. 3.8(a,d) shows the intact lattice and corresponding Fourier transform (FFT) depicts two distinct hexagons corresponding to graphene (blue) and MoS_2 (red) confirms that both materials are indeed present. To examine MoS_2 layer separately, the contamination (diffuse scattering) and graphene was filtered out from the images applying high-pass filter in the frequency domain, the results are shown in (Fig. 3.8(b)) and (Fig. 3.8(c)) from the image, respectively. A large scale image is presented in Fig. 3.8(e) which shows that there are no structural changes or perforation in either of the materials. These results strongly indicate that graphene shields MoS_2 against irradiation damage as it mitigates the induced ionization. However, it is worth pointing out that direct knock-on impact of heavy Xe ions could lead to sputtering of 1-4 atoms in MoS_2 lattice resulting in point defects [112]. Because

it is difficult to distinguish between very small irradiation and electron beam induced or intrinsic defects in STEM images, we only consider defects with sizes > 1 nm as irradiation damage or perforation. In graphene, point defects can react with for instance oxygen or hydrogen [115, 116], or become trapped under hydrocarbon contamination during sample transfer (in air) to STEM instrument and in MoS_2 or WS_2, bonded with oxygen and hydrogen [117, 118] or filled with contamination.

3.3 *In situ* STEM experiments

Results from *ex situ* manipulation of materials can only be observed afterwards in the microscope. If one wishes to observe the effects of the manipulation when it takes place, the experiment needs to be carried out *in situ*, inside a microscope. Such experiments can also provide insights into growth of materials. In this thesis, *in situ* experiments have been developed both for an individual low-dimensional materials and their heterostacks. We have focused on Joule-heating process to study the materials at high temperatures ($>$2000K).

3.3.1 Joule-heating of graphene

The content in this section corresponds to the fifth entry in the list of publications [5].

Typical samples of graphene and other 2D materials have residual contamination from the sample preparation and from the environment. One way to remove them would be annealing.

Ideally, graphene carries a high charge carrier mobility exceeding 200 000 cm^2/Vs [6] and thermal conductivity up to 4000 W/mK [33]. Thus, graphene is capable to carry high currents and sustain high thermal loads. Graphene temperature has shown to reach up to 2800 K at different bias voltages during Joule-heating [119]. The temperature-dependent thermal conductivity of graphene leads to reduced lateral heat dissipation and trapping of hot electrons at the center of graphene channel [120, 34, 121]. Previous studies have shown graphitization of polymer residues and amorphous carbon on graphene under electron irradiation and thermal annealing [122, 123, 124].

In this experiment, we fabricated a STEM-compatible suspended graphene device for *in situ* two probe measurements. The device consists of mechanically exfoliated graphene with two gold electrodes on a SiN membrane with a single hole. First, we exfoliated the monolayer

graphene onto a SiO_2/Si substrate. The source and drain electrodes were fabricated on the substrate using electron beam lithography and evaporation. Fig. 3.9(b) shows a light microscopy image of exfoliated graphene flake with two Au electrodes. Then, PMMA was spin-coated onto the assembly of graphene and electrodes at 4500 rpm and baked at 180°C for 2 min. The substrate was put in KOH solution to etch away the SiO_2 and thus separate the PMMA layer with graphene from the substrate subsequently transferred onto the SiN target substrate. The target substrate contained a hole of 3 μm and pre-defined electrodes created by photo-lithography, e-beam lithography and evaporation processes. The metal electrodes were used for aligning and guiding the graphene layer onto the target substrate. PMMA was locally cross-linked by high-dose electron irradiation to clamp both ends of graphene. Finally, PMMA residuals were dissolved into acetone, and rinsed in isopropanol. Fig. 3.9(a) depicts the device fabrication process. The process was finished with the critical point drying method to prevent the collapse of the structure. A light microscopy image of device structure is shown in Fig. 3.9(c). For *in situ* measurements, devices were loaded into the Nion electrical cartridge holder, which provides electrical terminals to apply an electric bias inside the microscope. We obtained current-voltage $(I - V)$ characteristics of graphene device inside the microscope.

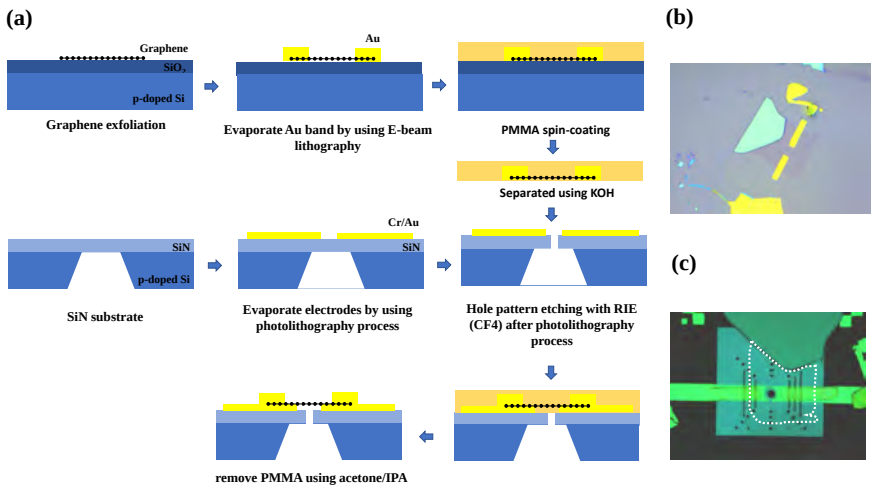

Figure 3.9: (a) Device fabrication process and light microscopy images of (b) exfoliated graphene flake with Au bands (c) device structure, graphene flake is highlighted with white dotted line.

Fig. 3.10(a) shows an overview (bright field CCD camera) image; the triangular markers work as guiders to find the sample in STEM. A STEM-MAADF image (Fig. 3.10(b)) shows the graphene device on which hydrocarbon contamination and some other residues are clearly visible. There is also crack which could have been produced due to tensile stress during the transfer or the fabrication process.

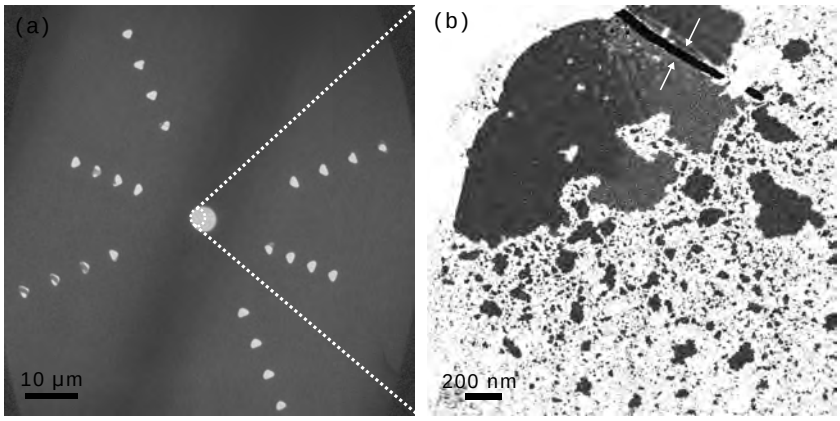

Figure 3.10: (a) Overview image of device structure (b) STEM-MAADF image of graphene from area marked in (a). White arrows in (b) indicates a crack in graphene lattice, formed during transfer process. From Ref. [92] Copyright 2020 Authors.

In the experiment, we applied several voltage sweeps across suspended graphene, while recording $I - V$ characteristics during each sweep. We observed that current increased until 1.0 V and then started to saturate (Fig. 3.14(a)), which indicates heating and thermal activation of optical phonons in the graphene membrane. No significant change in conductance was observed until 2.0 V during forward and backward sweeps. However, at sweep from 0.0 V to 3.0 V, a drastic increase was seen in the current at 2.2 V, and the saturation behavior also changed at 3.0 V. The estimated conductance was increased from 1.03x10^{-4} S to 5.06x10^{-4} S. This change could be explained with improvement in contacts with graphene, as thermal energy which can only be dissipated through the contact area can lead to thermal annealing and hence cleaning of the area. The dissipated power reached $\sim$2.0 mW at 3.0 V as shown in Fig. 3.14(b).

During the experiment, we monitored the dynamics of residual particles and other structural changes of the sample, as shown in Fig. 3.11. The STEM-images were acquired during voltage sweep from 2.5 V to 3 V. During these sweeps, we observed three dynamical processes: 1. movement and rotation of residual particles; 2. cleaning; and 3. widening of the crack. The image series in Fig. 3.11(a) shows the movement and rotation of a carbon-based residual particle marked with white arrows. The observed equilibrium positions are likely to be sites with high lattice disorder which makes them reactive. First, a bias voltage, the particle moves in two directions- along and perpendicular to the crack, and is likely to move along the direction of the electric field. Second, we observed a decrease in amount of residual material covering the graphene surface, or cleaning. Specifically, the bright contrast region, indicated with white arrow in the image series, gradually decreases (Fig. 3.11(b)). The high contrast regions were identified as PMMA and KOH residues with electron energy loss spectroscopy (Fig. 3.12). With increase in

temperature, bright contrast area transforms into dark contrast corresponding to clean graphene surface. This indicates the gradual cleaning of graphene at high temperatures.

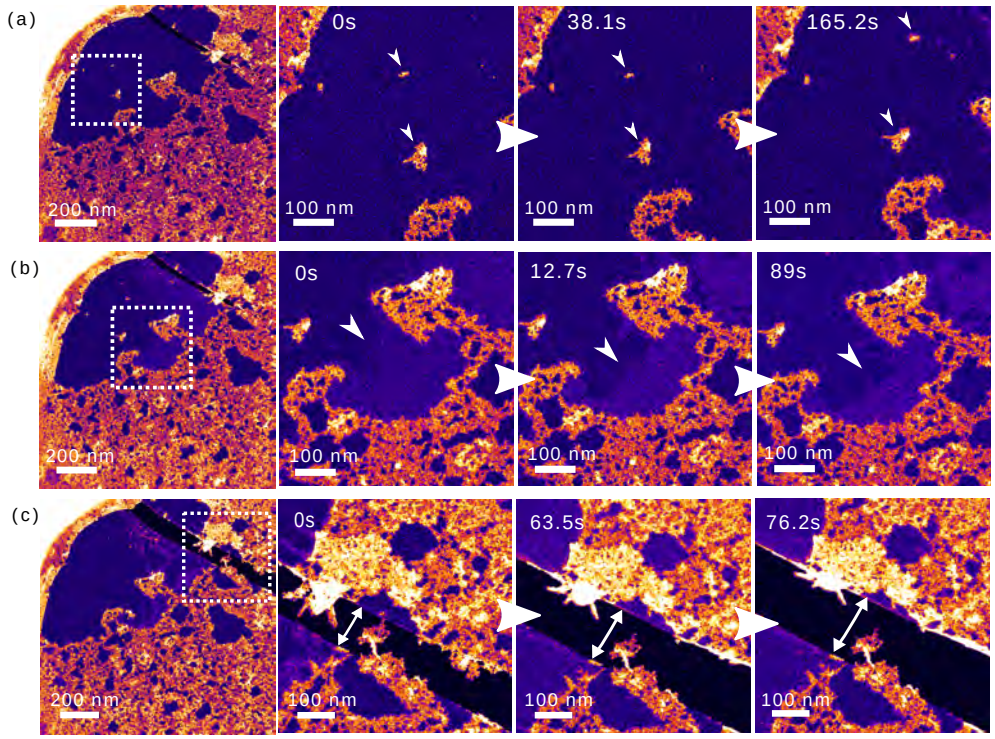

Figure 3.11: STEM-MAADF image series of dynamics of residual particles, cleaning and transformation on graphene surface. (a) Image series for rotation and translation of residual particles on graphene surface (b) Image series for dynamics of residual part (c) Image series for crack widening. Time stamped frames are closeup view from marked region in first frame of respective series. From Ref. [92] Copyright 2020 Authors.

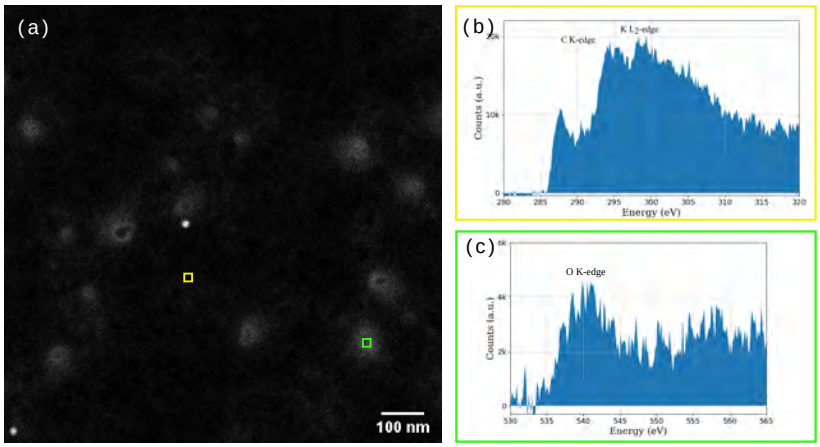

Figure 3.12: (a) STEM-HAADF image from the device. (b-c) Point spectra from the marked region in (a), showing the presence of oxygen and potassium residues. From Ref. [92] Copyright 2020 Authors.

COMSOL multiphysics simulations were used to estimate the temperature of the suspended graphene device as a function of bias voltage with electric and thermal transport in the channel, considering the Young's modulus of $E = 1.0$ TPa and value of 0.23 for Poisson's ratio. The thermal coefficient was assumed to be -8.0x10^{-6} K^{-1}. The geometry of the device was considered similar to the fabricated device described above, and the contact area with electrodes was defined as a heat sink. The highest temperature is at the middle of the channel, as lateral heat dissipation is reduced due to the temperature-dependent thermal conductivity. Fig. 3.13(a-e) illustrates the temperature distribution in the device. This reveals that temperature of device reaches up to 2000 K at 3 V (Fig. 3.13(f)).

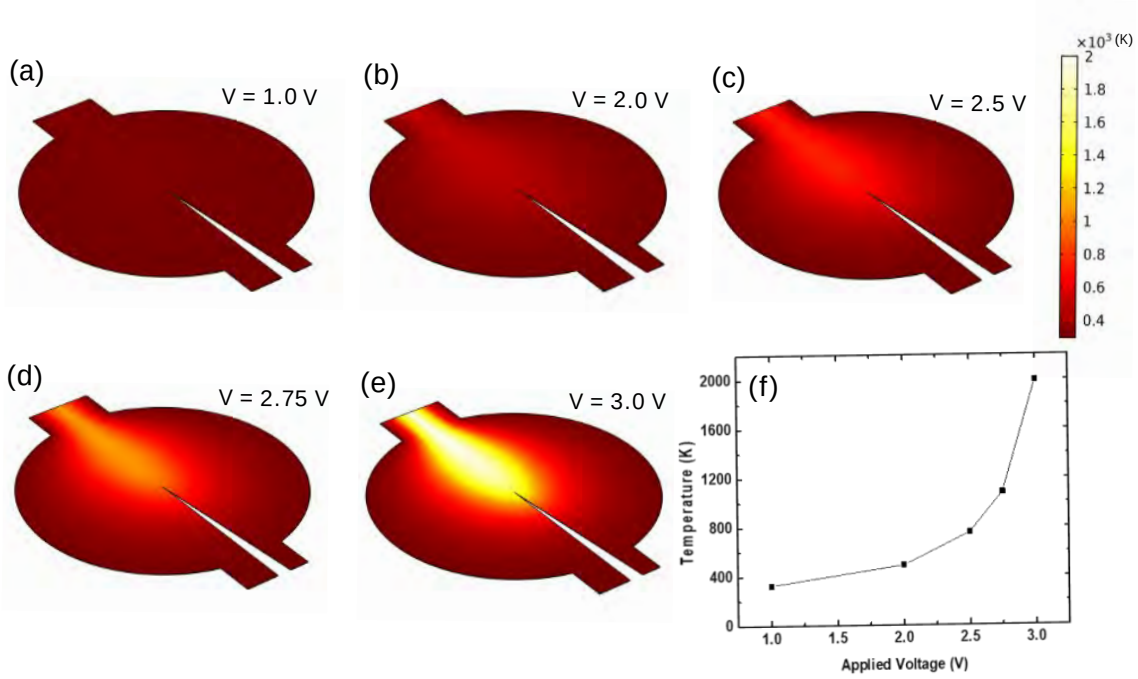

Figure 3.13: (a-e) Temperature distribution in graphene device estimated with simulations (f) Temperature variation as a function of applied voltage. From Ref. [92] Copyright 2020 Authors.

Lastly, we observed the the crack widening during Joule-heating process, as shown in Fig. 3.11(c). Since graphene has negative thermal coefficient, it should shrink with increasing temperature, which is in agreement with our observation. The maximum voltage of 8 V lead to tearing of graphene, which is an irreversible process and leads to a sudden drop in the current (Fig. 3.14(c-d)). This experiment suggests that graphene can be used as a conducting hot plate for other materials such as TMDs for observing their structural dynamics and evolution at high temperatures.

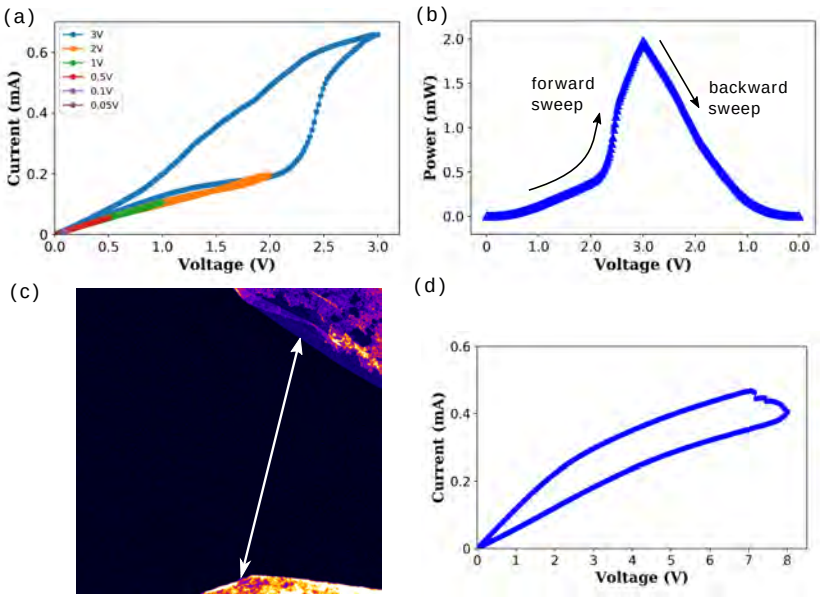

Figure 3.14: (a) Current-voltage characteristics recorded with a Keithley 2614B source meter during in-situ STEM observation of device (b) Power dissipated on device during voltage sweep between 0 V to 3 V (c) graphene was torn up at voltage of 8 V (d) I-V characteristics at 8V.

3.3.2 Joule-heating of graphene-MoS_2 heterostructures

The content in this section corresponds to the first entry in the list of publications [1].

In this experiment, we use a graphene hot plate for high temperature (up to 2800 K) experiments with MoS_2.

To fabricate the heterostructure device, we used CVD-grown MoS_2 and mechanically exfoliated graphene on SiO_2/Si substrate. To begin with, graphene substrate was spin coated with PMMA and dipped into KOH to get rid of SiO_2. The separated PMMA/graphene was transferred on MoS_2 and soaked into acetone for 1h to dissolve PMMA. Two gold electrodes were fabricated on the heterostructure followed by e-beam lithography and evaporation. Then, the as-fabricated heterostructure assembly with electrodes was placed on a customized electrical chip (Protochips) using the PMMA wet transfer method. The chip contained a 3x3 array of holes, each with a diameter of 5 μm, and four contact electrodes. The as-fabricated assembly was placed in a manner that the two electrodes overlapped with the existing electrodes. Finally, the chip was soaked in acetone to dissolve PMMA and rinsed in isopropanol. Fig. 3.15(a) depicts the device fabrication process and optical microscopy images of heterostructure on Si substrate and device are shown in Fig. 3.15(b-c). For *in situ* measurements, Nion UltraSTEM 100 microscope was operated at 60 kV acceleration voltage. Two probe measurements were carried out inside the microscope. Images were acquired with both MAADF and HAADF detectors.

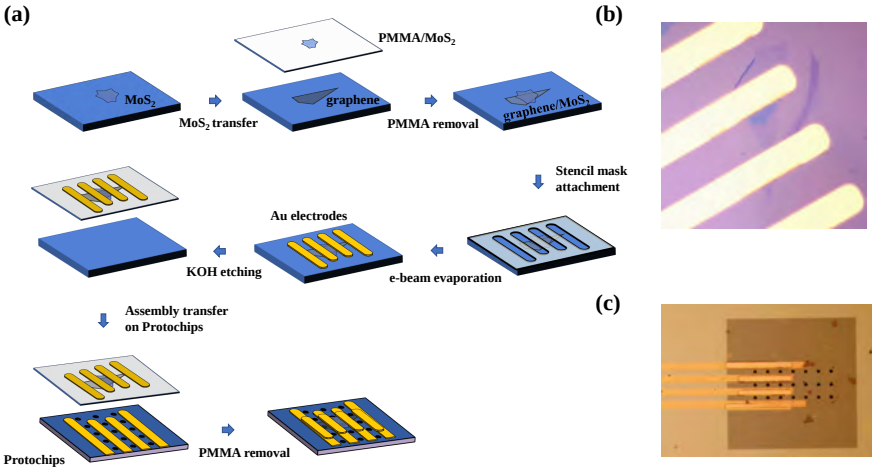

Figure 3.15: (a) Device fabrication process and light microscopy images of (b) graphene-MoS_2 heterostructure with Au electrodes on Si substrate (c) as fabricated device on Protochips.

Fig. 3.16(a) shows a low-magnification image of the device structure, and the hole marked with a white circle contains the graphene-MoS_2 heterostructure. An overview image of the device is shown in Fig. 3.16(b), where edge of monolayer MoS_2 is marked with a yellow line. This shows that MoS_2 covers half of the graphene-covered hole and is hence connected to only one of the electrodes at most. Fig. 3.16(c) shows a STEM-MAADF image from the selected part of Fig. 3.16(a). Fast Fourier transform (in inset) shows two distinct hexagons from graphene (green) and MoS_2 (yellow). The bright patches in the image are pockets in which hydrocarbon-based contamination is squeezed due to the van der Waals interaction between the two materials. A high-magnification image of interface is shown in Fig. 3.16(d) and atomically resolved images of graphene and MoS_2 from the marked rectangles in (d) are shown in Fig. 3.16(e-f), revealing that the MoS_2 has 1H structure. White circles indicate the S vacancy sites. The $I-V$ characteristics of the device display Ohmic behavior in Fig.3.16(g).

In Joule-heating process, we applied voltage sweeps in an increasing fashion across the two electrodes, recorded $I-V$ characteristics and acquired image sequences during each sweep to observe structural changes in the materials. In the beginning, we applied repeated voltage sweeps of 0 V-2 V to clean the surface, and simultaneously observed the interface under the combined effect of electron irradiation and Joule-heating. Since MoS_2 layer does not cover both electrodes, Joule-heating predominantly takes place in graphene and the heat is partially dissipiated to MoS_2, and the graphene thus acts as a hot-plate. This heating leads to the creation of sulfur vacancies within the MoS_2 basal plane, and the movement of Mo atoms at edges. Fig. 3.17 shows Mo-zigzag (ZZ) edges of MoS_2 layer on graphene. At 1.8 V, some of Mo atoms have moved on top

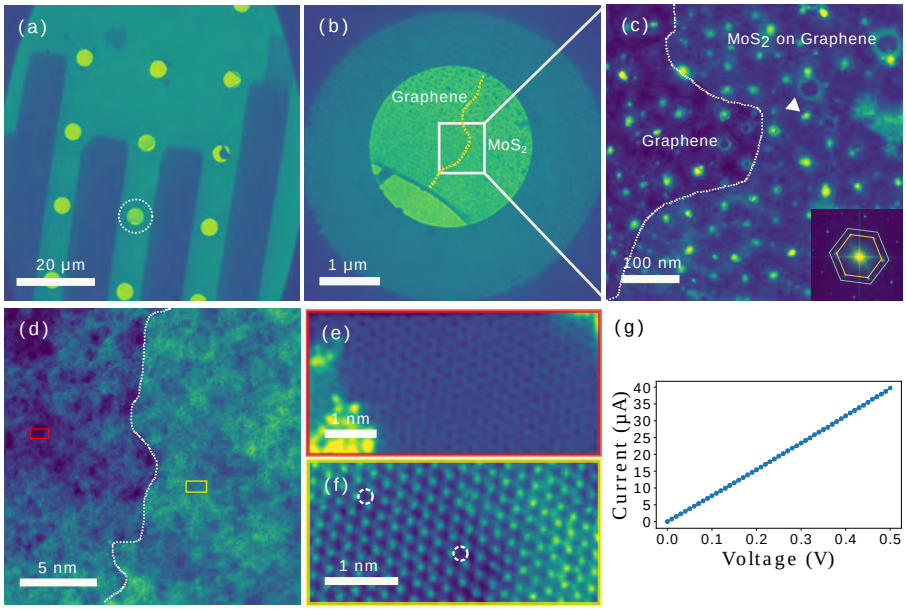

Figure 3.16: (a) Overview image of device structure, a hole marked with a white circle contains graphene and MoS_2. (b) Closeup view of hole marked in (a), suspended area of heterostructure. The yellow dashed line shows the edge of the MoS_2 layer. (c) STEM-MAADF image of graphene-MoS_2 interface, with the inset showing the corresponding FFT with graphene (green) and MoS_2 (yellow) spots marked with hexagons. (d) Higher-magnification image of the interface (e) Atomically resolved image of graphene from the red rectangle region in (d). (f) Atomically resolved image of MoS_2 from the yellow rectangle region in (d). The highlighted sites with white circles contain S vacancies. (g) Current-voltage characteristics of device at 0.5 V, showing the Ohmic behaviour. STEM images in panel (a) and (b) were acquired with the Ronchigram camera. From Ref. [125] Copyright 2021 Authors.

to form 3R polymorphs after the creation of sulfur vacancies. These changes at the edges are clearly visible in an image series shown in Fig. 3.17(a-c). On the other hand, we observed the gradual reduction of the area of contamination bubbles, as visible in the overview images shown in Fig. 3.17(d-f). Since graphene can sustain high current densities, a significant rise in the surface temperature and the evaporation and movement of contaminant residues on the surface is observed. At 1.8 V, some bubbles have completely disappeared, for instance one marked with a yellow arrow in Fig. 3.17(d-f). At 2 V, some line-like features are also visible, marked with white arrows in Fig. 3.17(f).

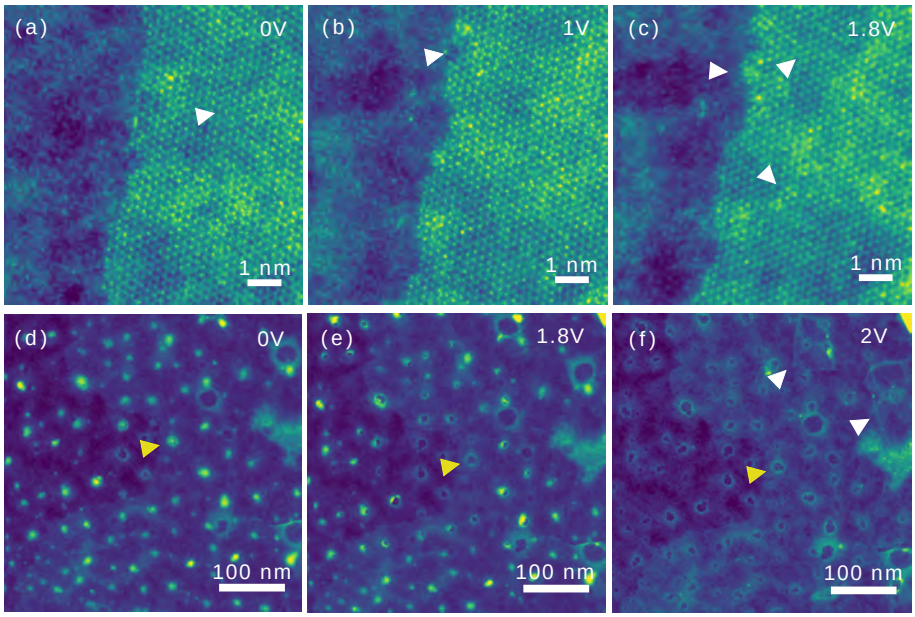

Figure 3.17: STEM-MAADF image series of edge evolution of MoS_2 and evaporation of contamination bubbles at bias voltages up to 2 V. (a-c) Image sequence obtained at different bias voltage. The white arrows are indicating the sulfur vacancy line and edge disorder. (d-f) Overview image sequence acquired after each voltage-sweep. White arrows mark line feature. All contamination bubbles have disappeared in (f). As an example, one bubble is marked with yellow arrow in sequence. From Ref. [125] Copyright 2021 Authors.

After increasing the bias voltage to 2.3 V, a nanopore appeared in MoS_2, which kept growing, and was followed by vacancy creation and cluster formation. This is an agreement with previous reports of vacancy formation and Mo agglomeration in MoS_2 at high temperatures [126, 63, 127]. The nanopore is marked with white arrow in Fig. 3.18(b-d). At a voltage of 2.7 V, the MoS_2 edge transformed into 1T' and Klein-like structures. Finally, at 3 V, the MoS_2 layer broke apart into nanoislands that transformed into nanocrystals at a much faster than that could be followed in real-time due to the very limited image acquisition rate. A maximum of 1.63 mW (3 V, 0.53 mA) power was dissipated on a 67.5 μm^2 slab of graphene which results in a power density of 2.4 x 10^7 W/m^2. A STEM-MAADF image series is shown in Fig. 3.18(a-h) that shows the pore formation and edge evaporation.

It is important to mention that the transformation happened all over the sample regardless of imaging area so this transition is clearly caused by heating alone and was not affected by electron irradiation. Numerical simulations of electrical and thermal transport predicted the temperature of graphene to reach 2800 K at 3 V [119]. However, due to asymmetric device geometry and uneven heat dissipation rate that follows, a thermal gradient must have existed on the suspended

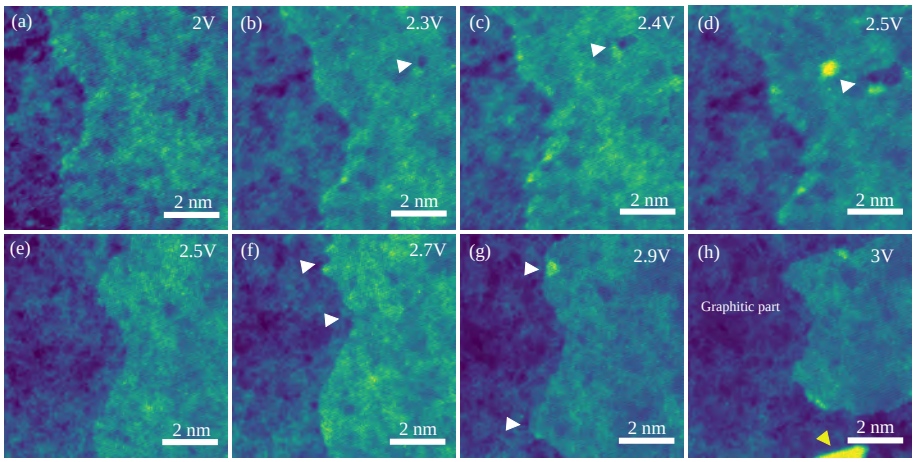

Figure 3.18: STEM-MAADF image sequence of pore formation and edge evaporation in MoS_2 at different voltages up to 3 V. Image sequence showing the formation and growth of nanopores and Mo agglomeration at the edges. The MoS_2 layer breaks apart as the voltage increases. White arrow marks nanopore and edge evaporation. Yellow arrow marks an individual crystal formed at 3 V in (h). From Ref. [125] Copyright 2021 Authors.

part of the sample. To display the effect of temperature gradient, we constructed a composite image of the device with several 2048×2048 nm^2 images, as shown in Fig. 3.19. In this image, upper part is clearly more cleaned than lower part. So, the upper part in the imaging geometry of sample is more affected than the lower part. (Fig. 3.20)

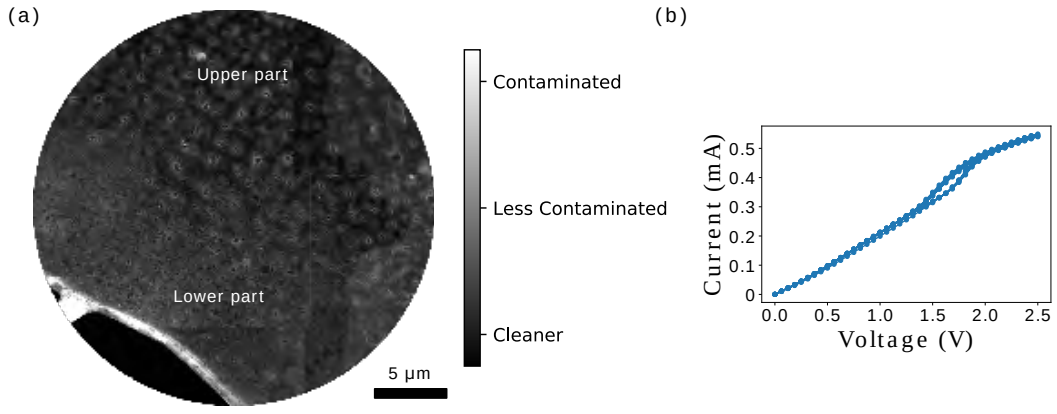

Figure 3.19: (a) STEM-MAADF overview (composite) image of the device, suspended area illustrating the clean and more contaminated ares after a voltage sweep up to 2.5 V, are marked with upper and lower part, respectively. Composite image is constructured with several 2048x2048 nm^2 images. (b) Corresponding $I - V$ characteristics. From Ref. [125] Copyright 2021 Authors.

The resulting nanocrystals show a variety of thicknesses, phases and heterointerfaces. To study the formation and dynamics of nanocrystals, we chose a nanoisland with a size of ca. 28 nm with mixed edge configurations, such as Mo-zigzag, Mo-klein, 1T'-like, and sulfur vacancies within its basal plane. We then apply repeated bias cycle between 2.3 V and 2.7 V, and recorded images to follow structural changes in the nanoisland. Fig. 3.20 depicts the step-by-step formation of nanocrystals. Upon biasing, we observed nanopore formation, void expansion, edge evaporation and clustering of Mo atoms at pore edges until the nanoisland completely disappeared and only dispersed nanocrystals were left on graphene surface. The nanocrystals exhibit predominantly a hexagonal shape with an average area of 16.75 nm^2.

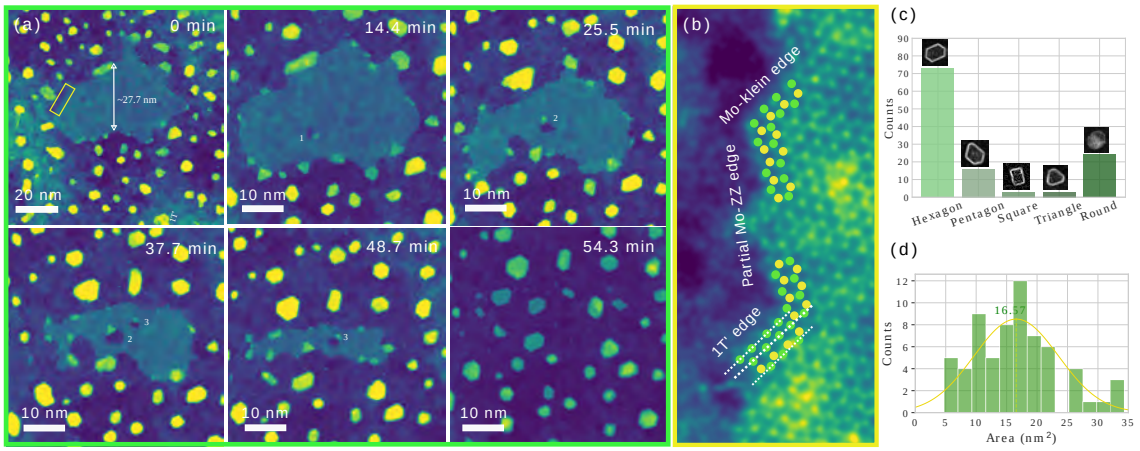

Figure 3.20: **Step-by-step formation of nanocrystals.** (a) STEM-MAADF image sequence of the step-by-step transformation of 2D MoS_2 island into 3D nanocrystals with repeated bias cycles up to 2.3 V-2.7 V. (b) Various configurations of the edge of the island from the location marked with yellow rectangle in first frame of (a). (c) Shape distribution of the freely dispersed crystals on graphene (d) Area distribution of freely dispersed hexagon crystals. From Ref. [125] Copyright 2021 Authors.

To discuss the morphology of nanocrystals, in Fig. 3.21, we selected a few crystals at the edges as the nanoislands with different phases and heterointerfaces. These crystals were intermediate structures during the transformation from 2D to 3D and hence provide insights into the formation of freely dispersed nanocrystals. Such crystals can form in different ways: 1. through folding of edges; 2. through migration of atoms on top, trapped at defect sites in the basal plane (inward growth); and 3. through migration at edges, nucleating outward growth. The nanocrystal shown in Fig. 3.21(a) presumably could have formed through inward growth, whereas Fig. 3.21(b) shows an example of a nanocrystal formed through folding of the edges. Other crystals look as if they would have grown outward. However, they must have grown inward as we never observed a crystal

formed outside the original nanoisland perimeter. The crystals show different shapes, sizes and phases. Fig. 3.21(a), for instance, shows a cluster with a triangular shape with Mo-ZZ and S-Klein-like edges, formed at a Mo-ZZ edge. Fig. 3.21(b) shows a polygon-shaped crystal with S-terminated and S-Klein like edges. In contrast, the other crystals have triangular or polygonal shapes with 2H, 1T and heterointerface 2H/3R, 2H/TZ structures, as shown in Fig. 3.21(c-e). As discussed earlier, after detaching from the 2D phase and emerging into 3D structures, most of crystals seem to attain a hexagonal shape. A hexagonal nanocrystal with the 2H structure is shown in Fig. 3.21(f). The composite FFT consisting spots from graphene, MoS_2 and a crystal (in inset) shows the orientation of the crystal on graphene surface. Chemical identification of crystals is shown in Fig. 3.22. There is no significant change in the $I-V$ characteristics of the device, indicating that the graphene and contacts remain largely unchanged during the transformation.

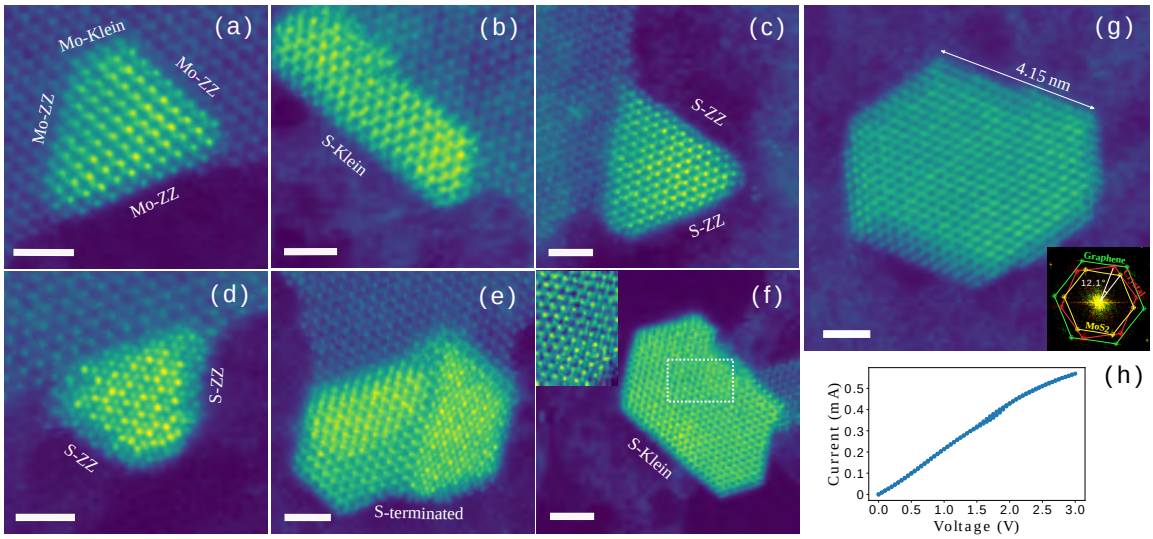

Figure 3.21: Selected nanocrystals with various phases. (a) A triangular 2H crystal (b) Polygonal 2H crystal (c) Triangular outward 2H and (d) 3R crystals. (e) 3R/TZ heterophase crystal. (f) 2H/TZ heterophase crystal (g) A freely dispersed hexagon-shaped 2H crystal. Inset shows composite Fourier transform from crystal (red) in (g), graphene (green) and MoS_2 (yellow), marked with hexagons (h) $I-V$ characteristics of the system during a voltage sweep up to 3 V. All STEM images were recorded with MAADF detector, except for (f), which was recorded with HAADF detector. The scale bars are 1 nm. From Ref. [125] Copyright 2021 Authors.

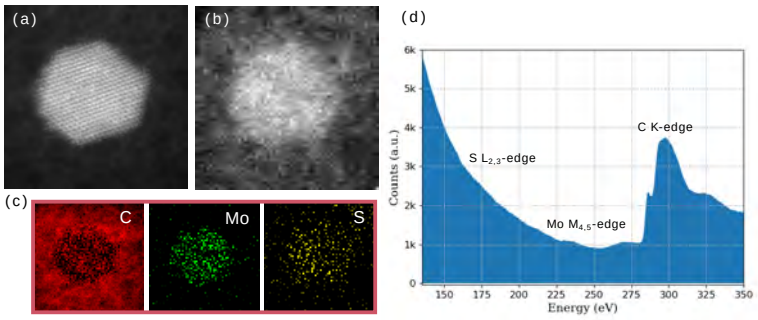

Figure 3.22: (a) STEM-HAADF image of a freely dispersed hexagon-shaped crystal (b) Corresponding HAADF image acquired during spectrum acquisition (c) Elemental mapping by selecting the energy range for each element's peak marked on the (d) EELS spectra. From Ref. [125] Copyright 2021 Authors.

3.3.3 Joule-heating of SWCNTs

The content in this section has not been published.

As further experiments during the thesis work that have not been published, we extended the concept of Joule heating to networks of SWCNTs. Electric current was passed through both sparse and dense networks. The former was supported on perforated SiN grids with pre-fabricated electrodes, whereas the latter one was entirely freestanding and allowed much higher temperatures to be accessed. Similar to graphene hot-plate, in these experiments a Keithley 2614B source meter was used to apply and record $I-V$ sweeps and structural dynamics taking place within the structure was observed *in situ*. The images were recorded with the Nion UltraSTEM instrument at 60 kV primary beam energy using the MAADF detector.

Two types of devices were fabricated in-house. The active area of the first device type comprised of an extremely thin network of SWCNTs with internal resistance in the order of 100 kOhms on a two-probe arrangement. The device was fabricated on a round TedPella Si grid with a 0.45×0.45 mm^2 freestanding perforated (hole size 2.5 μm) silicon nitride window by depositing nanotubes with thermophoresis as described previously.

Fig. 3.23 shows the STEM-MAADF image series of a sparse SWCNT network and the $I-V$ response at a varying bias range. The $I-V$ curves show liner, Ohmic behaviour around the zero-bias limit, slightly rectifying at higher bias values. Although the origin of the rectification is not entirely clear, it is likely emerging from the asymmetric, Schottky-like contacts between semiconducting SWCNTs and Au electrodes used to contact the device. Upon applying the bias cycle we also observed significant changes in the surface contamination.

Fig. 3.23(b) shows nanotubes are partially cleaned after bias cycle of -16 V to 16 V. Regardless of the high axial thermal conductivity, the center of the suspended part appears to be at a higher temperature. The clean areas are marked with white rectangles. At 22 V bias, the tubes are mostly cleaned (Fig. 3.23(c)). The difference in thermal expansion coefficients of silicon nitride and the graphitic carbon result in thermal strain that, when relaxed at room temperature, results in visible bends appearing on the nanotubes.

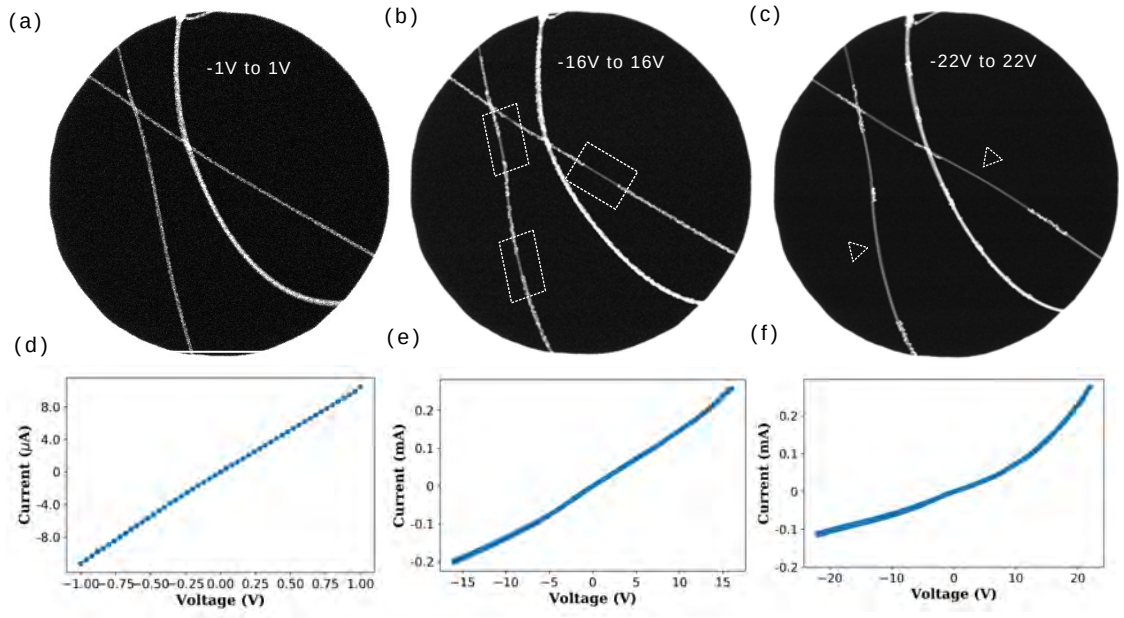

Figure 3.23: STEM-MAADF overview images of SWCNT networks (a) during sweep -1 V to 1 V (b) -16 V to 16 V and (c) -22 V to 22 V.

The second device type consisted of a dense network of nanotubes with internal resistance in the order of 250 Ohms. The size of the suspended area in this experiment was 600 μm$\times$100 μm, current and voltage applied through the structure reached 25 mA and 5.5 V, respectively and resulted in the maximum power density of 2.29 MW/m^2 that was dissipated on the freestanding film. Despite all efforts, the temperature could not be determined. Fig. 3.24 shows STEM-MAADF overview images of a pristine and Joule-heated network. The bright particles visible the first sub-panel on the left were identified to be iron using EELS. After the Joule annealing, both the amorphous contamination and iron particles were completely evaporated. The atomic resolution observations were carried out after each heating cycle and revealed, for instance, occasions where two SWCNTS were covalently merged as one. Fig. 3.24 shows an example of a (10,10) and (17,3) SWCNTs conjoining into a large carbon nanotube of an unknown structure.

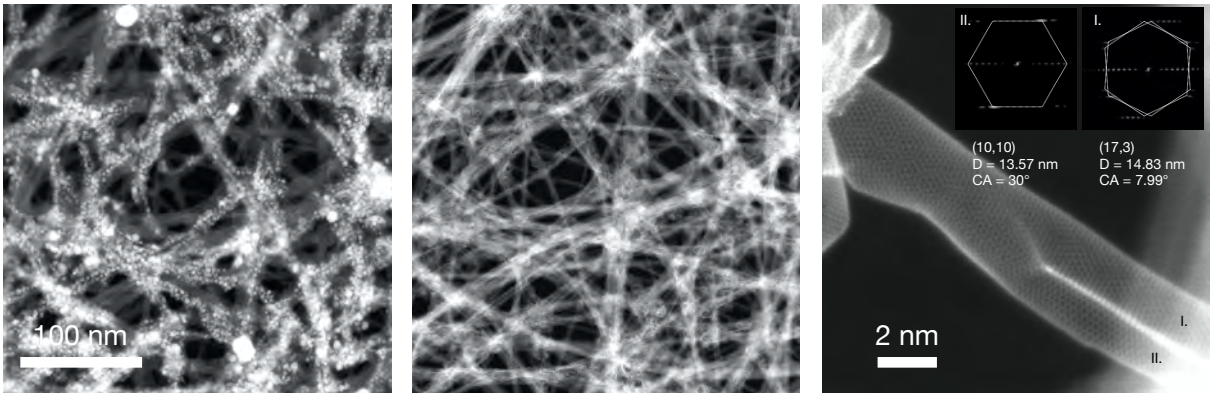

Figure 3.24: STEM-MAADF images of pristine and Joule-heated SWCNT networks and an atomically resolved image of a pair of (10,10) and (17,3) nanotubes.

Chapter 4

Conclusions and Outlook

In summary, in this thesis various possibilities to structurally modify low-dimensional solids via both *ex situ* and *in situ* means were studied. Together, the presented studies provide insights into nanostructuring techniques, structural manipulation, and transformation of stacked material systems, in some cases correlated with their electronic response. The work demonstrates foremostly the applicability of graphene as a general substrate for electron microscopy, allowing also high-temperature experiments far beyond what is achievable e.g. with silicon carbide-based heating substrates. In the first part, two *ex situ* methods were explored for manipulation of multidimensional heterostructures (1D/2D and 2D/2D), including plasma and highly charged ion irradiation. These studies demonstrated substitution of heteroatoms into SWCNTs/graphene and nanostructuring MoS_2 by creating nanopores. Next, we developed a method via *in situ* Joule-heating, in which temperatures as high as 2800 K can be generated by dissipating electric current in graphene, which thus allowed us to observing dynamics of surface contamination, and phase transformation of crystalline solids on a graphene hot plate.

Specifically, in the first study, we studied the modifications in SWCNTs/graphene heterostructures generated through Ar ion irradiation. The results showed substitution of Si heteroatoms into SWCNTs and graphene via intermittent vacancies created by the ions. In contrast to earlier experiments of similar type, continuous laser irradiation was successfully used to mitigate contamination buildup during ion irradiation. Since Si atoms are the most commonly found impurity species on graphene samples, laser heating released Si that migrated and filled some of the vacancies. The Si bonding configurations were further analyzed in SWCNTs and we observed that the atoms were mostly trapped into mono- and di-vacancy type defects similar to graphene, and with respective abundancies of 64% and 37%. The established method is universally applicable

for substitution of heteroatoms, although the success will depend on the availability of the target species and its diffusion rate (with respect to carbon adatoms) on graphene.

In the second part, nanostructuring of graphene-MoS_2 heterostructures using highly charged ion irradiation was studied. The samples were irradiated with 1.3 keV/amu Xe^{+38} ions. In particular, we studied the pore formation with either graphene or MoS_2 facing the ion beam, which allowed us to study both materials independently and their influence on one another. When ion beam facing the MoS_2, the results reveal the formation of nanometer-sized pores in MoS_2, whereas graphene beneath remained intact. This indicates that the potential energy was dissipated primarily in the first layers and the remainder was not enough to inflict damage in graphene. Indeed, it is also acknowledged that graphene is resistant to modifications upon HCI irradiation, which is believed to be due to its high carrier mobility. In this case, the pores in MoS_2 had an average radius of ca. 3.2 nm. In contrast, when the ion beam was facing graphene, no structural changes were observed in neither MoS_2 nor graphene, indicating a fast relaxation of electronic excitations in graphene and subsequent shielding of the MoS_2 layer.

In the last part, the graphene hot plate was used to study the dynamical structural transformations of amorphous material and MoS_2 at high temperatures. The first experiments were carried out with a simple device geometry of 2-point contacted and suspended graphene device. Upon cyclic electrical biasing, we observed dynamics of residual contamination particles on graphene. At high temperatures the particles tended to evaporate leading to cleaning of graphene surface. The cleaning was observed at an electric bias of ca. 3 V and was accompanied by rotation and movement of amorphous particles. The cleaning effect was correlated with a significant increase in 2-point conductance. Based on finite element simulations, we estimated that the temperature of graphene reached 2000 K at the maximum bias voltage of 3 V. This experiment indicates that the temperature of graphene can reach and sustain temperatures beyond 2000 K upon Joule-heating, allowing its utilization as a hot-plate for similar studies with other 2D materials. To bring this idea into its logical conclusions, we finally studied the dynamics of MoS_2 suspended on graphene monolayer in a heterostructure configuration. Upon applying bias cycles and due to the associated temperature rise, we observed the creation of sulfur vacancies in the MoS_2 basal plane. At around 3 V, the 2D layer gradually transformed into dispersed 3D nanocrystals followed by void creation and expansion and edge evaporation. These nanocrystals exhibit various structural phases and heterointerfaces with predominantly hexagonal shapes. The experiment provides insights into the evolution of TMDs materials at high temperatures, and may lead to applications utilizing dispersed nanocrystals with a uniform size distribution.

This work has established universal methods for structural modifications of materials and their stacked heterostructures. For example, substitution of atoms in single walled carbon nanotubes and graphene could be extended to heavy heteroatoms such as Al, Au and Ag etc. The highly charged ion irradiation can be used for nanostructuring of other TMDs materials (WS_2, $MoSe_2$, WSe_2 etc.) and their van der Waals heterostacked systems. Joule-heating processes need to be explored for an individual and combination of low-dimensional materials. These methods could give us insights in transformation and growth of materials. Moreover graphene "hot-plate" has a vital usability to observe the dynamics of materials at extreme high temperatures.

List of Publications

This list includes all peer-reviewed publications which I authored and co-authored during my PhD. They are ordered by publication date and I have mentioned my contribution for each of them. My contribution was crucial for publications 1, 3, 5 and 7 and are described in greater detail in the results chapter of the thesis.

1. **Step-by-step atomic insights into structural reordering from 2D to 3D MoS_2**
   Heena Inani, Dong Hoon Shin, Jacob Madsen, Hyunjeong Jeong, Min Hee Kwon, Niall McEvoy, Toma Susi, Clemens Mangler, Sang Wook Lee, Kimmo Mustonen, and Jani Kotakoski
   Advanced Functional Materials, 31, 2008395 (2021)
   Author Contributions: H.I. carried out all STEM experiments, analyzed the data and wrote the first draft of the manuscript.

2. **Highly efficient bilateral doping of single-walled carbon nanotubes**
   Anastasia E Goldt, Orysia T Zaremba, Mikhail O Bulavskiy, Fedor S Fedorov, Konstantin V Larionov, Alexey P Tsapenko, Zakhar I Popov, Pavel Sorokin, Anton S Anisimov, **Heena Inani**, Jani Kotakoski, Kimmo Mustonen, Albert G Nasibulin
   Journal of Materials Chemistry C, DOI: 10.1039/d0tc05996j (2021)
   Author Contributions: H.I. collected the STEM data.

3. **Atomic-scale carving of nanopores into a van der Walls heterostructure with slow highly charged ions**
   Janine Schwestka*, **Heena Inani***, Mukesh Tripathi, Anna Niggas, Niall McEvy, Florian Libisch, Freidrich Aumayr, Jani Kotakoski and Richard A. Willhelm
   ACS Nano, 14, 8, 10536-10543 (2020)
   *J.S. and **H.I.** contributed equally.
   Author Contributions: H.I. prepared the samples, carried out all STEM experiments and analyzed the data.

4. **Vanishing influence of the band gap on the charge exchange of slow highly charged ions in freestanding single-layer MoS_2**

   S Creutzburg, J Schwestka, A Niggas, **H Inani**, M Tripathi, A George, R Heller, R Kozubek, L Madauß, N McEvoy, S Facsko, J Kotakoski, M Schleberger, A Turchanin, PL Grande, F Aumayr, RA Wilhelm

   Physics Review B,102, 045508 (2020)

   Author Contributions: H.I. prepared the samples with the help of M.T. for TEM study.

5. **Transformation and evaporation of surface adsorbents on a graphene "Hot Plate"**

   Jun Hee Choi, Dong Hoon Shin, **Heena Inani**, Min Hee Kwon, Kimmo Mustonen, Clemens Mangler, Min Park, Hyunjeong Jeong, Dong Su Lee, Jani Kotakoski, and Sang Wook Lee

   ACS Applied Materials Interfaces, 12, 23 (2020)

   Author Contributions: H.I. carried out the experiment, collected and analyzed the data and prepared few figures for the manuscript.

6. **Electron-beam manipulation of silicon impurities in single-walled carbon nanotubes**

   Kimmo Mustonen, Alexander Markevich, Mukesh Tripathi, **Heena Inani**, Er-Xiong Ding, Aqueel Hussain, Clemens Mangler, Esko I. Kauppinen, Jani Kotakoski and Toma Susi

   Advanced Functional Materials, 29, 1901327 (2019)

   Author Contributions: H.I. prepared the sample and performed plasma irradiation experiment and supported in collecting the data.

7. **Silicon substitution in nanotubes and graphene via intermittent vacancies**

   Heena Inani, Kimmo Mustonen, Alexander Markevich, Er-Xiong Ding, Mukesh Tripathi, Aqueel Hussain, Clemens Mangler, Esko I. Kauppinen, Toma Susi and Jani Kotakoski

   Journal of Physical Chemistry C, 123, 20 (2019)

   Author Contributions: H.I. prepared the sample, performed plasma irradiation experiments, collected and analyzed the data and wrote the first draft of the manuscript.

Contributions to scientific events

Participation in international conferences:

Date & Venue	Conference	Type	Title of contribution
February 5-10, 2018 & Obergurgl, Austria	Graphene Study		
July 9-13, 2018 & Trieste, Italy	Conference on Physics of Defects in Solids: Quantum Mechanics Meets Topology	Poster	Atomic Scale Investigations of 1D-2D Heterostructures
August 27-29, 2018 & Belgrade, Serbia	Electron Microscopy of Nanostructures (ELMINA) Conference	Poster	Atomic Scale Investigations of 1D-2D Heterostructures
February 12-14, 2019 & Levi, Finland	Towards Reality in Nanoscale Materials X (TRNM)	Poster	Substituting Si in Graphene and Carbon Nanotubes through Intermittent Vacancies
July 21-26, 2019 & Würzburg, Germany	NT19: International Conference on the Science and Application of Nanotubes and Low-Dimensional Materials	Poster	Substitutional Si Doping of Graphene and Nanotubes through Ion Irradiation-Induced Vacancies
August 4-8, 2019 & Portland, USA	Microscopy and Microanalysis (M&M) 2019	Oral	Substitutional Si Doping of Graphene and Nanotubes through Ion Irradiation-Induced Vacancies
November 27-December 4, 2020 & Boston, USA	2020 Virtual MRS Spring/Fall Meeting & Exhibit	Oral	*In situ* High Temperature Dynamics of Surface Residues and Monolayer MoS_2 on Graphene Surface

Bibliography

[1] Peierls, R. Quelques propriétés typiques des corps solides. *Annales de l'I.H.P.* **5**, 177–222 (1935).

[2] L.D. Landau & E.M. Lifshitz. *STATISTICAL PHYSICS, PART I, Sections 137 and 138* (Pergamon, Oxford, 1980).

[3] Mermin, N. D. Crystalline Order in Two Dimensions. *Physical Review* **176**, 250–254 (1968). DOI: 10.1103/PhysRev.176.250.

[4] Zinke-Allmang, M., Feldman, L. C. & Grabow, M. H. Clustering on surfaces. *Surface Science Reports* **16**, 377–463 (1992). DOI: 10.1016/0167-5729(92)90006-W.

[5] Evans, J. W., Thiel, P. A. & Bartelt, M. C. Morphological evolution during epitaxial thin film growth: Formation of 2D islands and 3D mounds. *Surface Science Reports* **61**, 1–128 (2006). DOI: 10.1016/j.surfrep.2005.08.004.

[6] Novoselov, K. S. Electric Field Effect in Atomically Thin Carbon Films. *Science* **306**, 666–669 (2004). DOI: 10.1126/science.1102896.

[7] Novoselov, K. S. *et al.* A roadmap for graphene. *Nature* **490**, 192–200 (2012). DOI: 10.1038/nature11458.

[8] Novoselov, K. S., Mishchenko, A., Carvalho, A. & Castro Neto, A. H. 2D materials and van der Waals heterostructures. *Science* **353**, aac9439 (2016). DOI: 10.1126/science.aac9439.

[9] Duesberg, G. S. Heterojunctions in 2D semiconductors: A perfect match. *Nature Materials* **13**, 1075–1076 (2014). DOI: 10.1038/nmat4127.

[10] Wilson, N. R. *et al.* Determination of band offsets, hybridization, and exciton binding in 2D semiconductor heterostructures. *Science Advances* **3**, e1601832 (2017). DOI: 10.1126/sciadv.1601832.

[11] Jariwala, D., Marks, T. J. & Hersam, M. C. Mixed-dimensional van der Waals heterostructures. *Nature Materials* **16**, 170–181 (2017). DOI: 10.1038/nmat4703.

[12] Blackburn, J. L. *et al.* Synthesis and characterization of boron-doped single-wall carbon nanotubes produced by the laser vaporization technique. *Chemistry of Materials* **18**, 2558–2566 (2006). DOI: 10.1021/cm060192i.

[13] Campos-Delgado, J. *et al.* Chemical vapor deposition synthesis of N-, P-, and Si-doped single-walled carbon nanotubes. *ACS Nano* **4**, 1696–1702 (2010). DOI: 10.1021/nn901599g.

[14] Bangert, U. *et al.* Ion implantation of graphene - Toward IC compatible technologies. *Nano Letters* **13**, 4902–4907 (2013). DOI: 10.1021/nl402812y.

[15] Su, C. *et al.* Engineering single-atom dynamics with electron irradiation. *Science Advances* **5**, 2252 (2019). DOI: 10.1126/sciadv.aav2252.

[16] Zhou, W. *et al.* Direct determination of the chemical bonding of individual impurities in graphene. *Physical Review Letters* **109**, 2–6 (2012). DOI: 10.1103/PhysRevLett.109.206803.

[17] Tripathi, M. *et al.* Implanting Germanium into Graphene. *ACS Nano* **12**, 4641–4647 (2018). DOI: 10.1021/acsnano.8b01191.

[18] Kozubek, R. *et al.* Perforating Freestanding Molybdenum Disulfide Monolayers with Highly Charged Ions. *Journal of Physical Chemistry Letters* **10**, 904–910 (2019). DOI: 10.1021/acs.jpclett.8b03666.

[19] Gruber, E. *et al.* Ultrafast electronic response of graphene to a strong and localized electric field. *Nature Communications* **7**, 13948 (2016). DOI: 10.1038/ncomms13948.

[20] Lin, Y.-C., Dumcenco, D. O., Huang, Y.-S. & Suenaga, K. Atomic mechanism of the semiconducting-to-metallic phase transition in single-layered MoS2. *Nature Nanotechnology* **9**, 391–396 (2014). DOI: 10.1038/nnano.2014.64.

[21] Lin, J., Pantelides, S. T. & Zhou, W. Vacancy-induced formation and growth of inversion domains in transition-metal dichalcogenide monolayer. *ACS Nano* **9**, 5189–5197 (2015). DOI: 10.1021/acsnano.5b00554.

[22] Ly, T. H., Zhao, J., Cichocka, M. O., Li, L.-J. & Lee, Y. H. Dynamical observations on the crack tip zone and stress corrosion of two-dimensional MoS2. *Nature Communications* **8**, 14116 (2017). DOI: 10.1038/ncomms14116.

[23] Lin, J. *et al.* Flexible metallic nanowires with self-adaptive contacts to semiconducting transition-metal dichalcogenide monolayers. *Nature Nanotechnology* **9**, 436–442 (2014). DOI: 10.1038/nnano.2014.81.

[24] Masih Das, P. *et al.* Controlled Sculpture of Black Phosphorus Nanoribbons. *ACS Nano* **10**, 5687–5695 (2016). DOI: 10.1021/acsnano.6b02435.

[25] Sang, X. *et al.* In situ edge engineering in two-dimensional transition metal dichalcogenides. *Nature Communications* **9**, 2051 (2018). DOI: 10.1038/s41467-018-04435-x.

[26] Tai, K.-l. *et al.* Atomic-Scale Fabrication of In-Plane Heterojunctions of Few-Layer MoS 2 via In Situ Scanning Transmission Electron Microscopy. *Small* **16**, 1905516 (2020). DOI: 10.1002/smll.201905516.

[27] Wallace, P. R. The Band Theory of Graphite. *Physical Review* **71**, 622–634 (1947). DOI: 10.1103/PhysRev.71.622.

[28] Castro Neto, A. H., Guinea, F., Peres, N. M. R., Novoselov, K. S. & Geim, A. K. The electronic properties of graphene. *Reviews of Modern Physics* **81**, 109–162 (2009). DOI: 10.1103/RevModPhys.81.109.

[29] Lee, C., Wei, X., Kysar, J. W. & Hone, J. Measurement of the Elastic Properties and Intrinsic Strength of Monolayer Graphene. *Science* **321**, 385–388 (2008). DOI: 10.1126/science.1157996.

[30] Novoselov, K. S. *et al.* Two-dimensional atomic crystals. *Proceedings of the National Academy of Sciences* **102**, 10451–10453 (2005). DOI: 10.1073/pnas.0502848102.

[31] Mucciolo, E. R. & Lewenkopf, C. H. Disorder and electronic transport in graphene. *Journal of Physics: Condensed Matter* **22**, 273201 (2010). DOI: 10.1088/0953-8984/22/27/273201.

[32] Peres, N. M. Graphene: New physics in two dimensions. *Europhysics News* **40**, 17–20 (2009). DOI: 10.1051/epn/2009501.

[33] Balandin, A. A. Thermal properties of graphene and nanostructured carbon materials. *Nature Materials* **10**, 569–581 (2011). DOI: 10.1038/nmat3064.

[34] Pop, E., Varshney, V. & Roy, A. K. Thermal properties of graphene: Fundamentals and applications. *MRS Bulletin* **37**, 1273–1281 (2012). DOI: 10.1557/mrs.2012.203.

[35] Kim, K. *et al.* High-temperature stability of suspended single-layer graphene. *Physica Status Solidi - Rapid Research Letters* **4**, 302–304 (2010). DOI: 10.1002/pssr.201000244.

[36] Manzeli, S., Ovchinnikov, D., Pasquier, D., Yazyev, O. V. & Kis, A. 2D transition metal dichalcogenides. *Nature Reviews Materials* **2**, 17033 (2017). DOI: 10.1038/natrevmats.2017.33.

[37] Cui, H., Guo, Y., Ma, W. & Zhou, Z. 2 D Materials for Electrochemical Energy Storage: Design, Preparation, and Application. *ChemSusChem* **13**, 1155–1171 (2020). DOI: 10.1002/cssc.201903095.

[38] Birmingham, B. *et al.* Spatially-Resolved Photoluminescence of Monolayer MoS2 under Controlled Environment for Ambient Optoelectronic Applications. *ACS Applied Nano Materials* **1**, 6226–6235 (2018). DOI: 10.1021/acsanm.8b01422.

[39] Radisavljevic, B., Whitwick, M. B. & Kis, A. Integrated circuits and logic operations based on single-layer MoS 2. *ACS Nano* **5**, 9934–9938 (2011). DOI: 10.1021/nn203715c.

[40] Voiry, D. *et al.* Conducting MoS2 nanosheets as catalysts for hydrogen evolution reaction. *Nano Letters* **13**, 6222–6227 (2013). DOI: 10.1021/nl403661s.

[41] Li, H. *et al.* From bulk to monolayer MoS2: Evolution of Raman scattering. *Advanced Functional Materials* **22**, 1385–1390 (2012). DOI: 10.1002/adfm.201102111.

[42] Splendiani, A. *et al.* Emerging photoluminescence in monolayer MoS2. *Nano Letters* **10**, 1271–1275 (2010). DOI: 10.1021/nl1903868w.

[43] Goate & APP. ©19 9 1 Nature Publishing Group. *Letters To Nature* **353**, 737–740 (1991).

[44] Odom, T. W., Huang, J. L., Kim, P. & Lieber, C. M. Structure and Electronic Properties of Carbon Nanotubes. *Journal of Physical Chemistry B* **104**, 2794–2809 (2000). DOI: 10.1021/jp993592k.

[45] Zhang, Y. J. *et al.* Optoelectronic response of a WS 2 tubular p - n junction. *2D Materials* **5**, 035002 (2018). DOI: 10.1088/2053-1583/aab670.

[46] Zhang, Y. J. *et al.* Enhanced intrinsic photovoltaic effect in tungsten disulfide nanotubes. *Nature* **570**, 349–353 (2019). DOI: 10.1038/s41586-019-1303-3.

[47] Levi, R., Bitton, O., Leitus, G., Tenne, R. & Joselevich, E. Field-effect transistors based on WS2 nanotubes with high current-carrying capacity. *Nano Letters* **13**, 3736–3741 (2013). DOI: 10.1021/nl401675k.

[48] Sugahara, M. *et al.* Ambipolar transistors based on random networks of WS2 nanotubes. *Applied Physics Express* **9**, 075001 (2016). DOI: 10.7567/APEX.9.075001.

[49] Koma, A. Van der Waals epitaxy - a new epitaxial growth method for a highly lattice-mismatched system. *Thin Solid Films* **216**, 72–76 (1992). DOI: 10.1016/0040-6090(92)90872-9.

[50] Liu, Y. *et al.* Van der Waals heterostructures and devices. *Nature Reviews Materials* **1**, 16042 (2016). DOI: 10.1038/natrevmats.2016.42.

[51] Mustonen, K. A. *et al.* Atomic-Scale Deformations at the Interface of a Mixed-Dimensional van der Waals Heterostructure. *ACS Nano* **12**, 8512–8519 (2018). DOI: 10.1021/acsnano.8b04050.

[52] Liao, M. *et al.* Twist angle-dependent conductivities across MoS2/graphene heterojunctions. *Nature Communications* **9**, 4068 (2018). DOI: 10.1038/s41467-018-06555-w.

[53] Pomerantseva, E. & Gogotsi, Y. Two-dimensional heterostructures for energy storage. *Nature Energy* **2**, 17089 (2017). DOI: 10.1038/nenergy.2017.89.

[54] Liu, Y. *et al.* Planar carbon nanotube-graphene hybrid films for high-performance broadband photodetectors. *Nature Communications* **6**, 1–7 (2015). DOI: 10.1038/ncomms9589.

[55] Furchi, M. M. *et al.* Device physics of van der Waals heterojunction solar cells. *npj 2D Materials and Applications* **2**, 3 (2018). DOI: 10.1038/s41699-018-0049-3.

[56] Lee, J., Shin, J.-H., Lee, G.-H. & Lee, C.-H. Two-Dimensional Semiconductor Optoelectronics Based on van der Waals Heterostructures. *Nanomaterials* **6**, 193 (2016). DOI: 10.3390/nano6110193.

[57] Bangert, U. *et al.* Ion Implantation of Graphene—Toward IC Compatible Technologies. *Nano Letters* **13**, 4902–4907 (2013). DOI: 10.1021/nl402812y.

[58] Yamamoto, K., Kamimura, T. & Matsumoto, K. Nitrogen Doping of Single-Walled Carbon Nanotube by Using Mass-Separated Low-Energy Ion Beams. *Japanese Journal of Applied Physics* **44**, 1611–1614 (2005). DOI: 10.1143/JJAP.44.1611.

[59] Hatakeyama, R., Jeong, G. H. & Hirata, T. Material incorporation inside single-walled carbon nanotubes using plasma-ion irradiation method. *IEEE Transactions on Nanotechnology* **3**, 333–342 (2004). DOI: 10.1109/TNANO.2004.828517.

[60] Khare, B. *et al.* Functionalization of Carbon Nanotubes via Nitrogen Glow Discharge. *The Journal of Physical Chemistry B* **109**, 23466–23472 (2005). DOI: 10.1021/jp0537254.

[61] Bayer, B. C. *et al.* Atomic-scale in situ observations of crystallization and restructuring processes in two-dimensional MoS2 films. *ACS Nano* **12**, 8758–8769 (2018). DOI: 10.1021/acsnano.8b04945.

[62] Komsa, H.-P., Kurasch, S., Lehtinen, O., Kaiser, U. & Krasheninnikov, A. V. From point to extended defects in two-dimensional MoS2: Evolution of atomic structure under electron irradiation. *Physical Review B* **88**, 035301 (2013). DOI: 10.1103/PhysRevB.88.035301.

[63] Huang, W., Wang, X., Ji, X., Zhang, Z. & Jin, C. In-situ fabrication of Mo6S6-nanowire-terminated edges in monolayer molybdenum disulfide. *Nano Research* **11**, 5849–5857 (2018). DOI: 10.1007/s12274-018-2089-6.

[64] Zhou, Y. *et al.* Grain Boundaries as Electrical Conduction Channels in Polycrystalline Monolayer WS2. *ACS Applied Materials and Interfaces* **11**, 10189–10197 (2019). DOI: 10.1021/acsami.8b21391.

[65] Li, H. *et al.* Activating and optimizing MoS2 basal planes for hydrogen evolution through the formation of strained sulphur vacancies. *Nature Materials* **15**, 48–53 (2016). DOI: 10.1038/nmat4465.

[66] Grønborg, S. S. *et al.* Visualizing hydrogen-induced reshaping and edge activation in MoS2 and Co-promoted MoS2 catalyst clusters. *Nature Communications* **9**, 2211 (2018). DOI: 10.1038/s41467-018-04615-9.

[67] Schleberger, M. & Kotakoski, J. 2D Material Science: Defect Engineering by Particle Irradiation. *Materials* **11**, 1885 (2018). DOI: 10.3390/ma11101885.

[68] Madauß, L. *et al.* Defect engineering of single- and few-layer MoS 2 by swift heavy ion irradiation. *2D Materials* **4**, 015034 (2016). DOI: 10.1088/2053-1583/4/1/015034.

[69] Thiruraman, J. P., Masih Das, P. & Drndić, M. Irradiation of Transition Metal Dichalcogenides Using a Focused Ion Beam: Controlled Single-Atom Defect Creation. *Advanced Functional Materials* **29**, 1904668 (2019). DOI: 10.1002/adfm.201904668.

[70] Wilhelm, R. *et al.* Neutralization Dynamics of Slow Highly Charged Ions in 2D Materials. *Applied Sciences* **8**, 1050 (2018). DOI: 10.3390/app8071050.

[71] Li, Z. & Chen, F. Ion beam modification of two-dimensional materials: Characterization, properties, and applications. *Applied Physics Reviews* **4**, 011103 (2017). DOI: 10.1063/1.4977087.

[72] Singh, J. *Fundamentals of Light Microscopy and Electronic Imaging*, vol. 68 (1994).

[73] Gaede. Das Elektronenmikroskop. *Deutsche Medizinische Wochenschrift* **66**, 858–860 (1940). DOI: 10.1055/s-0028-1122268.

[74] von Ardenne, M. Das Elektronen-Rastermikroskop - Theoretische Grundlagen. *Zeitschrift für Physik* **109**, 553–572 (1938). DOI: 10.1007/BF01341584.

[75] Scherzer, O. ber einige Fehler von Elektronenlinsen. *Zeitschrift fr Physik* **101**, 593–603 (1936). DOI: 10.1007/BF01349606.

[76] Crewe, A. V., Wall, J. & Welter, L. M. A high-resolution scanning transmission electron microscope. *Journal of Applied Physics* **39**, 5861–5868 (1968). DOI: 10.1063/1.1656079.

[77] Zach, J. & Haider, M. Aberration correction in a low voltage SEM by a multipole corrector. *Nuclear Inst. and Methods in Physics Research, A* **363**, 316–325 (1995). DOI: 10.1016/0168-9002(95)00056-9.

[78] Haider, M. *et al.* A spherical-aberration-corrected 200 kV transmission electron microscope. *Ultramicroscopy* **75**, 53–60 (1998). DOI: 10.1016/S0304-3991(98)00048-5.

[79] Krivanek, O. L., Delby, N., Spence, A. J., Camps, R. A. & Brown, L. M. Aberration correction in the STEM. In *Inst. Phys. Conf. Ser. EMAG97*, vol. 153, 35–40 (1997).

[80] Krivanek, O. L., Dellby, N., Spence, A. J., Camps, R. A. & Michael Brown, L. On-Line Aberration Measurement and Correction in STEM. *Microscopy and Microanalysis* **3**, 1171–1172 (1997). DOI: 10.1017/S1431927600012745.

[81] Krivanek, O., Dellby, N. & Lupini, A. Towards sub-Å electron beams. *Ultramicroscopy* **78**, 1–11 (1999). DOI: 10.1016/S0304-3991(99)00013-3.

[82] Haigh, S. J. & Kirkland, A. I. Aberration-Corrected Imaging in CTEM. In *Aberration-Corrected Analytical Transmission Electron Microscopy* (John Wiley & Sons, Ltd, Chichester, UK, 2011).

[83] Krivanek, O. L. *et al.* An electron microscope for the aberration-corrected era. *Ultramicroscopy* **108**, 179–195 (2008). DOI: 10.1016/j.ultramic.2007.07.010.

[84] Hotz, M. *et al.* Ultra-High Vacuum Aberration-Corrected STEM for in-situ studies. *Microscopy and Microanalysis* **22**, 34–35 (2016). DOI: 10.1017/s1431927616001021.

[85] Krivanek, O. L. *et al.* Atom-by-atom structural and chemical analysis by annular dark-field electron microscopy. *Nature* **464**, 571–574 (2010). DOI: 10.1038/nature08879.

[86] Egerton, R. F. Electron energy-loss spectroscopy in the TEM. *Reports on Progress in Physics* **72**, 016502 (2009). DOI: 10.1088/0034-4885/72/1/016502.

[87] Pantelic, R. S., Meyer, J. C., Kaiser, U. & Stahlberg, H. The application of graphene as a sample support in transmission electron microscopy. *Solid State Communications* **152**, 1375–1382 (2012). DOI: 10.1016/j.ssc.2012.04.038.

[88] Lin, X. *et al.* Development of an ultra-thin film comprised of a graphene membrane and carbon nanotube vein support. *Nature Communications* **4**, 2920 (2013). DOI: 10.1038/ncomms3920.

[89] Nair, R. R. *et al.* Graphene as a transparent conductive support for studying biological molecules by transmission electron microscopy. *Applied Physics Letters* **97**, 153102 (2010). DOI: 10.1063/1.3492845.

[90] Wojcik, M., Hauser, M., Li, W., Moon, S. & Xu, K. Graphene-enabled electron microscopy and correlated super-resolution microscopy of wet cells. *Nature Communications* **6**, 7384 (2015). DOI: 10.1038/ncomms8384.

[91] Westenfelder, B. *et al.* Graphene-based sample supports for in situ high-resolution TEM electrical investigations. *Journal of Physics D: Applied Physics* **44**, 055502 (2011). DOI: 10.1088/0022-3727/44/5/055502.

[92] Choi, J. H. *et al.* Transformation and Evaporation of Surface Adsorbents on a Graphene "Hot Plate". *ACS Applied Materials & Interfaces* **12**, 26313–26319 (2020). DOI: 10.1021/acsami.0c02056.

[93] Tripathi, M. *et al.* Cleaning graphene: Comparing heat treatments in air and in vacuum. *physica status solidi (RRL) - Rapid Research Letters* **11**, 1700124 (2017). DOI: 10.1002/pssr.201700124.

[94] Muñoz, R. & Gómez-Aleixandre, C. Review of CVD synthesis of graphene. *Chemical Vapor Deposition* **19**, 297–322 (2013). DOI: 10.1002/cvde.201300051.

[95] Jung, Y., Ji, E., Capasso, A. & Lee, G.-H. Recent Progresses in the Growth of Two-dimensional Transition Metal Dichalcogenides. *Journal of the Korean Ceramic Society* **56**, 24–36 (2019). DOI: 10.4191/kcers.2019.56.1.12.

[96] Ramakrishna Matte, H. S. *et al.* MoS2 and WS2 analogues of graphene. *Angewandte Chemie - International Edition* **49**, 4059–4062 (2010). DOI: 10.1002/anie.201000009.

[97] Terranova, M. L., Sessa, V. & Rossi, M. The world of carbon nanotubes: An overview of CVD growth methodologies. *Chemical Vapor Deposition* **12**, 315–325 (2006). DOI: 10.1002/cvde.200600030.

[98] Ding, E. X. *et al.* Highly conductive and transparent single-walled carbon nanotube thin films from ethanol by floating catalyst chemical vapor deposition. *Nanoscale* **9**, 17601–17609 (2017). DOI: 10.1039/c7nr05554d.

[99] Laiho, P., Mustonen, K., Ohno, Y., Maruyama, S. & Kauppinen, E. I. Dry and Direct Deposition of Aerosol-Synthesized Single-Walled Carbon Nanotubes by Thermophoresis. *ACS Applied Materials and Interfaces* **9**, 20738–20747 (2017). DOI: 10.1021/acsami.7b03151.

[100] Conrads, H. & Schmidt, M. Plasma generation and plasma sources. *Plasma Sources Science and Technology* **9**, 441–454 (2000). DOI: 10.1088/0963-0252/9/4/301.

[101] Panagopoulos, T. & Economou, D. J. Plasma sheath model and ion energy distribution for all radio frequencies. *Journal of Applied Physics* **85**, 3435–3443 (1999). DOI: 10.1063/1.369701.

[102] Tolvanen, A., Kotakoski, J., Krasheninnikov, A. V. & Nordlund, K. Relative abundance of single and double vacancies in irradiated single-walled carbon nanotubes. *Applied Physics Letters* **91**, 173109 (2007). DOI: 10.1063/1.2800807.

[103] Schwestka, J. On the Charge Exchange Dynamics of Highly Charged Ions in Atomically Thinly Solids (2020).

[104] Ramasse, Q. M. *et al.* Probing the bonding and electronic structure of single atom dopants in graphene with electron energy loss spectroscopy. *Nano Letters* **13**, 4989–4995 (2012). DOI: 10.1021/nl304187e.

[105] Inani, H. *et al.* Silicon Substitution in Nanotubes and Graphene via Intermittent Vacancies. *The Journal of Physical Chemistry C* **123**, acs.jpcc.9b01894 (2019). DOI: 10.1021/acs.jpcc.9b01894.

[106] Krasheninnikov, A. V., Banhart, F., Li, J. X., Foster, A. S. & Nieminen, R. M. Stability of carbon nanotubes under electron irradiation: Role of tube diameter and chirality. *Physical Review B* **72**, 125428 (2005). DOI: 10.1103/PhysRevB.72.125428.

[107] Susi, T. *et al.* Silicon–Carbon Bond Inversions Driven by 60-keV Electrons in Graphene. *Physical Review Letters* **113**, 115501 (2014). DOI: 10.1103/PhysRevLett.113.115501.

[108] Geim, A. K. & Grigorieva, I. V. Van der Waals heterostructures. *Nature* **499**, 419–425 (2013). DOI: 10.1038/nature12385.

[109] Zhao, X. *et al.* Engineering and modifying two-dimensional materials by electron beams. *MRS Bulletin* **42**, 667–676 (2017). DOI: 10.1557/mrs.2017.184.

[110] Susi, T., Meyer, J. C. & Kotakoski, J. Quantifying transmission electron microscopy irradiation effects using two-dimensional materials. *Nature Reviews Physics* **1**, 397–405 (2019). DOI: 10.1038/s42254-019-0058-y.

[111] Kretschmer, S., Lehnert, T., Kaiser, U. & Krasheninnikov, A. V. Formation of Defects in Two-Dimensional MoS2 in the Transmission Electron Microscope at Electron Energies below the Knock-on Threshold: The Role of Electronic Excitations. *Nano Letters* **20**, 2865–2870 (2020). DOI: 10.1021/acs.nanolett.0c00670.

[112] Ghorbani-Asl, M., Kretschmer, S., Spearot, D. E. & Krasheninnikov, A. V. Two-dimensional MoS 2 under ion irradiation: from controlled defect production to electronic structure engineering. *2D Materials* **4**, 025078 (2017). DOI: 10.1088/2053-1583/aa6b17.

[113] Elibol, K. *et al.* Atomic Structure of Intrinsic and Electron-Irradiation-Induced Defects in MoTe2. *Chemistry of Materials* **30**, 1230–1238 (2018). DOI: 10.1021/acs.chemmater.7b03760.

[114] Schwestka, J. *et al.* Atomic-Scale Carving of Nanopores into a van der Waals Heterostructure with Slow Highly Charged Ions. *ACS Nano* **14**, 10536–10543 (2020). DOI: 10.1021/acsnano.0c04476.

[115] Zan, R., Ramasse, Q. M., Bangert, U. & Novoselov, K. S. Graphene reknits its holes. *Nano Letters* **12**, 3936–3940 (2012). DOI: 10.1021/nl300985q.

[116] Vijayasekhar, K., Acharyya, S. G., Debroy, S., Miriyala, V. P. K. & Acharyya, A. Self-healing phenomena of graphene: Potential and applications. *Open Physics* **14**, 364–370 (2016). DOI: 10.1515/phys-2016-0040.

[117] Pető, J. *et al.* Spontaneous doping of the basal plane of MoS 2 single layers through oxygen substitution under ambient conditions. *Nature Chemistry* **10**, 1246–1251 (2018). DOI: 10.1038/s41557-018-0136-2.

[118] Cochrane, K. A. *et al.* Intentional carbon doping reveals CH as an abundant charged impurity in nominally undoped synthetic WS 2 and WSe 2. *2D Materials* **7**, 031003 (2020). DOI: 10.1088/2053-1583/ab8543.

[119] Kim, Y. D. *et al.* Bright visible light emission from graphene. *Nature Nanotechnology* **10**, 676–681 (2015). DOI: 10.1038/nnano.2015.118.

[120] Pop, E. *et al.* Negative Differential Conductance and Hot Phonons in Suspended Nanotube Molecular Wires. *Physical Review Letters* **95**, 155505 (2005). DOI: 10.1103/PhysRevLett.95.155505.

[121] Nika, D. L., Pokatilov, E. P., Askerov, A. S. & Balandin, A. A. Phonon thermal conduction in graphene: Role of Umklapp and edge roughness scattering. *Physical Review B* **79**, 155413 (2009). DOI: 10.1103/PhysRevB.79.155413.

[122] Huang, J. Y. *et al.* In-situ observation of graphene sublimation and edge reconstructions. *Microscopy and Microanalysis* **15**, 1164–1165 (2009). DOI: 10.1017/S1431927609092678.

[123] Huang, J. Y., Qi, L. & Li, J. In situ imaging of layer-by-layer sublimation of suspended graphene. *Nano Research* **3**, 43–50 (2010). DOI: 10.1007/s12274-010-1006-4.

[124] Westenfelder, B. *et al.* Transformations of carbon adsorbates on graphene substrates under extreme heat. *Nano Letters* **11**, 5123–5127 (2011). DOI: 10.1021/nl203224z.

[125] Inani, H. *et al.* Step-By-Step Atomic Insights into Structural Reordering from 2D to 3D MoS 2. *Advanced Functional Materials* **31**, 2008395 (2021). DOI: 10.1002/adfm.202008395.

[126] Chen, Q. *et al.* Ultralong 1D vacancy channels for rapid atomic migration during 2d void formation in monolayer MoS2. *ACS Nano* **12**, 7721–7730 (2018). DOI: 10.1021/acsnano.8b01610.

[127] Chen, J. *et al.* In situ high temperature atomic level dynamics of large inversion domain formations in monolayer MoS2. *Nanoscale* **11**, 1901–1913 (2019). DOI: 10.1039/c8nr08821g.